

Article

Petrogenesis and Geochronology of A₁-Type Rhyolites in the Late Late Triassic of the East Kunlun Orogenic Belt: Constraints on the End of the Paleo-Tethys Orogenic Event

Zuochen Li ^{1,2,*}, Xianzhi Pei ^{1,2,*}, Lei Pei ^{1,2}, Chengjun Liu ^{1,2}, Lili Xu ^{1,2}, Ruibao Li ^{1,2}, Hao Lin ¹, Mao Wang ¹, Shang Ji ¹, Li Qin ¹, Yajie Yang ¹, Meng Wang ^{1,2}, Shaowei Zhao ^{1,2} and Youxin Chen ^{1,2}

¹ Key Laboratory of Western China's Mineral Resources and Geological Engineering, Ministry of Education, School of Earth Science and Resources, Chang'an University, Xi'an 710054, China

² Xi'an Key Laboratory for Mineralization and Efficient Utilization of Critical Metals, Xi'an 710054, China

* Correspondence: lizuochen@chd.edu.cn (Z.L.); peixzh@sina.com (X.P.)

Abstract: The rhyolites which are widely exposed to the northern margin of the East Kunlun orogenic belt were chosen as a research object to discern the post-orogenic tectonic evolution of the East Kunlun orogenic belt and reconstruct the post-collision orogenic processes of the Buquingshan-A'nyemaqen Ocean. We researched zircon U-Pb ages and geochemistry characteristics of the Late Triassic rhyolites in the eastern segment of the East Kunlun Orogenic Belt in the northern Tibetan Plateau. Zircon U-Pb dating yields coeval ages of 200.4 ± 1.4 Ma and 202.8 ± 1.2 Ma for the Keri rhyolites of the East Kunlun Orogenic Belt, indicating that the volcanic rocks were formed in the Late Triassic Rhaetian–Early Jurassic Hettangian. The Keri rhyolite is a product of the late magmatism of the Elashan Formation volcanic rocks. The rhyolites include rhyolitic brecciated tuff lavas and rhyolitic tuff lavas. The rhyolites are peraluminous and are high-K calc-alkaline, with high contents of SiO₂, K₂O, TFe₂O₃, and low P₂O₅ contents. The A/CNK ratios range from 0.97 to 1.09, indicating that the rhyolites are metaluminous to weakly peraluminous. The chondrite-normalized rare earth element (REE) distribution shows a significant negative Eu anomaly and low total REE concentrations. All samples are depleted in high field strength elements (HFSEs, e.g., Eu, Sr, Ti, and P), heavy rare earth elements (HREEs), and enriched in large ion lithophile elements (LILEs, e.g., Rb, Zr, Nd, Th, and U) and light rare earth elements (LREEs). The Keri rhyolite has the characteristics of A₁-type magmatic rock, formed in an anorogenic environment after the closure of the Paleo-Tethys Ocean, and was the product of late magmatism in the Elashan Formation volcanic rocks.

Keywords: geochronology; geochemistry; east Kunlun orogenic belt; petrogenesis; rhyolites; Paleo-Tethys ocean

Citation: Li, Z.; Pei, X.; Pei, L.; Liu, C.; Xu, L.; Li, R.; Lin, H.; Wang, M.; Ji, S.; Qin, L.; et al. Petrogenesis and Geochronology of A₁-Type Rhyolites in the Late Late Triassic of the East Kunlun Orogenic Belt: Constraints on the End of the Paleo-Tethys Orogenic Event. *Minerals* **2023**, *13*, 290. <https://doi.org/10.3390/min13020290>

Academic Editor: Stefano Salvi

Received: 12 January 2023

Revised: 2 February 2023

Accepted: 16 February 2023

Published: 18 February 2023



Copyright: © 2023 by the authors. Submitted for possible open access publication under the terms and conditions of the Creative Commons Attribution (CC BY) license (<https://creativecommons.org/licenses/by/4.0/>).

1. Introduction

The East Kunlun Orogenic Belt (EKOB), an important part of the central orogenic system of China, is located in the northern part of the Qinghai–Tibet Plateau and in the southern part of the Qaidam Basin (Figure 1). It is a giant tectonic igneous belt comparable to the Gangdese igneous belt in the Qinghai–Tibet Plateau. This belt is oriented E–W with a length of more than 800 km, a width of approximately 40–80 km, and an exposed area of approximately 50,000 km² [1–4]. The belt lies at the suture between the North China Block and the Yangtze Block [5–8]. The EKOB is a complex continental orogenic belt with a unique tectonic evolutionary history with multiple stages of tectonism. As it experienced several tectonic phases, the EKOB is crucial to better understanding the tectonic evolution of the entire region. Igneous rocks, such as the abundant granitoid intrusions, can provide insight into the evolution of this Paleo-Tethys system.

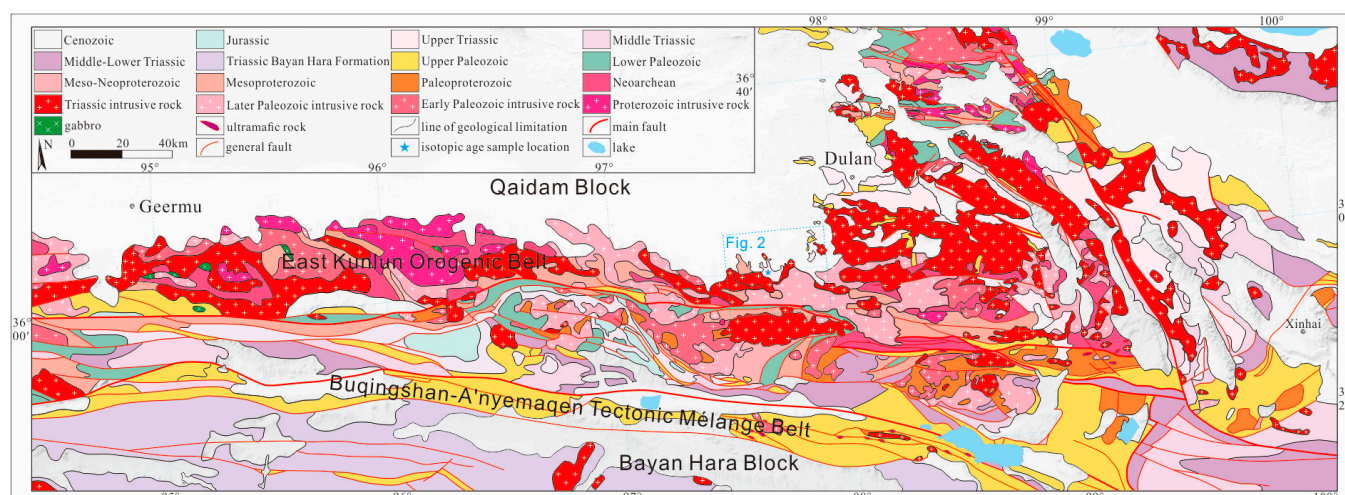


Figure 1. Map showing the regional context of the EKOB. Light blue rectangle outlines the area shown in Figure 2. Geological map modified from Li et al. [1]. Topographic map data: accessed on <https://map.tianditu.gov.cn/>.

The EKOB is a composite continental orogenic belt that has experienced multistage tectonism with a complex and distinct tectonic evolution history. The Early–Middle Triassic granitoids are mainly distributed in the north part of the EKOB, especially along the East Kunlun Fault. The south part of the EKOB, including the Bayan Hara, Bugingshan-A'nyemaqen, and Qiangtang units, is less exposed [9,10]. Each granite phase has a slightly different outcrop pattern, reflecting the structural evolution of the area. Based on the research of sedimentation, igneous activity, and metamorphism, Liu et al. [9] divided the EKOB into four major geological tectonic cycles: Precambrian, Cambrian to Middle Devonian, Late Devonian to Late Triassic, and Early Jurassic to present [11]. Among them, the Late Paleozoic to Early Mesozoic orogenic event (i.e., the Variscan–Indosinian orogenic cycle) is the best-established and the especially important orogenic cycle in the region [8,12]. At present, researchers are trying to analyze the subduction process of the Paleo-Tethyan Ocean through the large number of Triassic granites in the EKOB [3,8,13–41]. The massive distribution of intrusive rocks in the East Kunlun region plays a key role in the sequence of tectonic events in this area. The widespread and massive distribution of intrusive rocks are critical to the sequence of magmatic–tectonic events in this area. The volcanic rocks represented by the combination of basic–intermediate–acidic of Elashan Formation volcanic rocks were exposed in the northern margin of the East Kunlun in the Late Triassic [38,42–53]. The acidic volcanic rocks were the products of the final stage of magma evolution and were an important part of continental igneous processes including an active continental margin, a continental rift, and a large igneous province [54–58]. The study of its genesis is crucial to understanding the evolution of continental crust in this region [59].

Therefore, this paper focuses on the upper rhyolite of the Elashan Formation to explore its petrogenesis, magma sources, and tectonic setting through zircon U–Pb geochronology, geochemistry, and petrographic analyses to provide constraints for further discussion on the formation and evolution of the Triassic and the end time of Triassic orogeny in the EKOB Paleotethys Ocean.

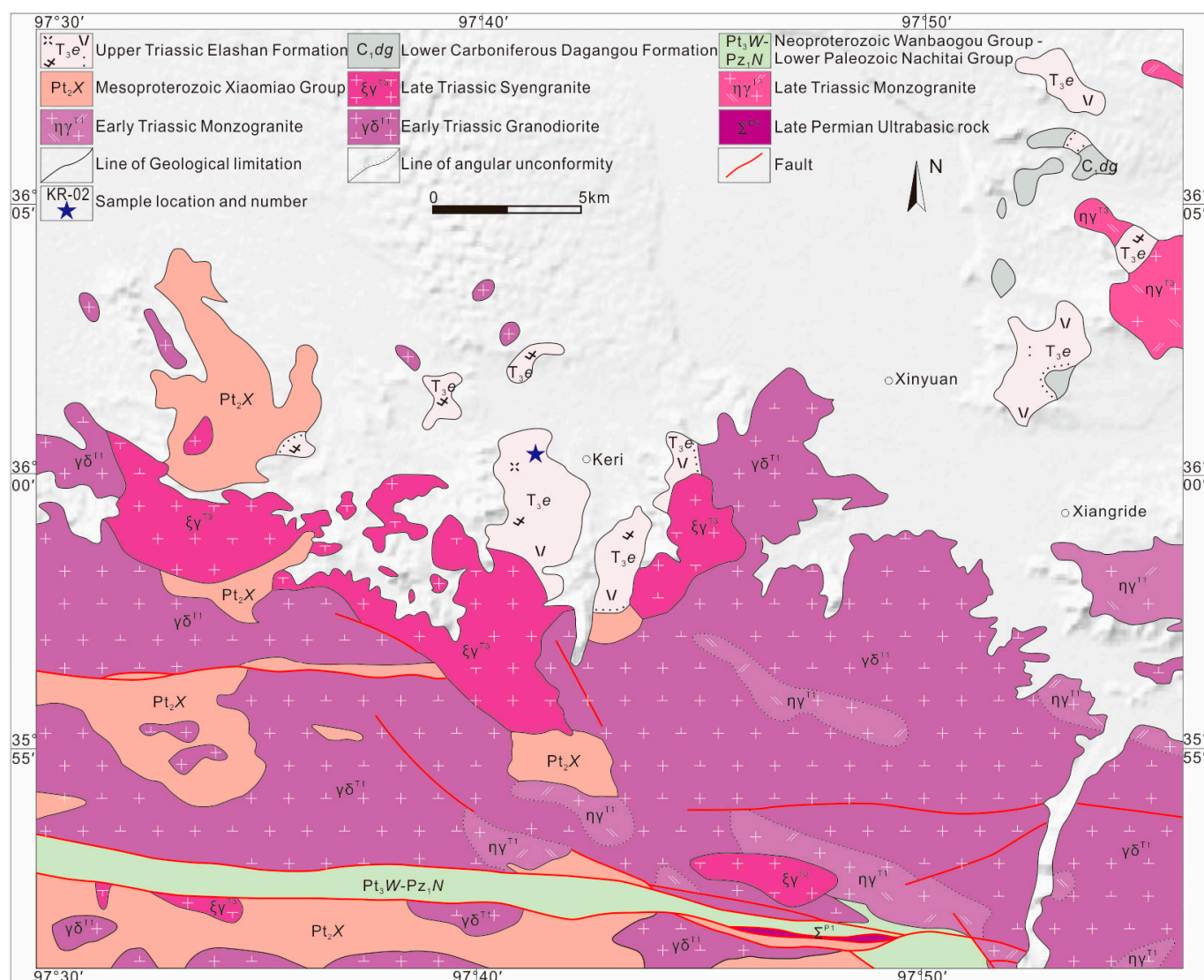


Figure 2. Map showing the regional geological of the Keri rhyolites in the EKOB. Geological map after Yin et al. [60]; Topographic map data: accessed on <https://map.tianditu.gov.cn/>.

2. Geological Background

The Elashan Formation is distributed on the southeast margin of Qaidam Block and is unconformable with a set of volcanoclastic rocks with volcanic lava and sedimentary clastic rocks on the underlying strata and/or intrusions [42] (Figure 2). The Elashan Formation is a set of purple, dark purple, gray green, and other variegated volcanoclastic rocks mainly containing volcanic lava, sedimentary clastic rocks, and a large number of exotic blocks (limestone). In general, the lower layers are dominated by intermediate and basic volcanic rocks interspersed with clastic rocks. The middle layer is an intermediate-acidic gray green dacite lava tuff. The upper layer is mainly composed of acidic volcanic rocks interspersed with clastic rocks and increased lava. Therefore, the Elashan Formation is mainly composed of intermediate-acidic volcanic rocks (Figure 3a,b), and the top and bottom are missing in most areas. The volcanic rocks are characterized by flow structures, columnar joints, with red tops and green bottoms (Figure 3c).



Figure 3. Field photographs and photomicrographs of the Keri rhyolites in the EKOB. (a,b) Field photographs of the Keri rhyolites; (c) columnar joints of rhyolitic tuff lavas; (d) field photos of the rhyolitic brecciated tuff lavas.

3. Petrography

The Elashan Formation volcanic rocks in the Keri area of the EKOB are mainly rhyolitic brecciated tuff lavas (Figure 3d) and rhyolitic tuff lavas (Figure 3c).

The rhyolitic brecciated tuff lavas are light grayish red, purplish-red, and gray in color with brecciated tuff lava textures, with spherulite (Figure 4a), and massive in structure. The rubble (approximately 18%) is mainly composed of rhyolite, quartz, and K-feldspar, with minor quartzite and plastic debris in the breccias. Blastofelsic spherulites are colorless and transparent with obvious cross-extinction phenomenon. Blastofelsic spherulites have obvious cross-extinction in the microscope. There are many cores, and the core is common with crystal nucleus (Figure 4b). The individual grain size is between 0.5 and 3 mm. Most of them have 2–3 layers of autogenous enlarged bands, and often appear as multiple spheroids in a dumbbell shape. The debris is intermediate–acidic volcanic rocks (mainly acidic volcanic rock), mostly in subangular and subcircular shape, mainly semi-plastic debris, with a grain size of < 2 mm and a content of 30%. The crystals and porphyrites are unevenly distributed and contain quartz, K-feldspar, and plagioclase. Crystals (angular to subangular) and phenocrysts are often corroded. The corrosion of quartz includes corrosion bays and perforations, accounting for 10%–15%. Feldspar has calcite alteration, and individual feldspar are strongly altered. The matrices in the lava include pyroclast (debris, crystal) and phenocrysts. The matrix minerals are fine-grained, with microcrystalline structure mainly composed of feldspar (main) and quartz (secondary), with a content of 40%–45%, and secondary sericite (main) and calcite (less), with a content of 10%.

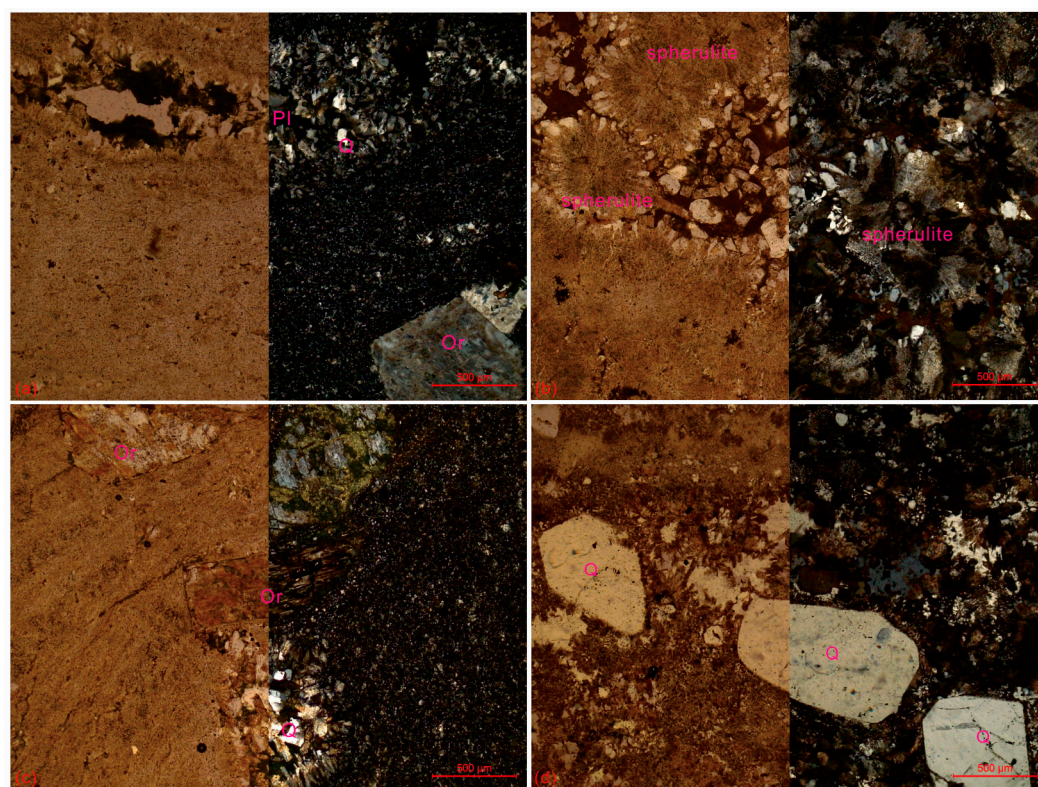


Figure 4. Photomicrographs of the Keri rhyolites in the EKOB. (a) Photomicrographs of the rhyolitic brecciated tuff lavas (sample XRD110-6); (b) spherulite texture of the rhyolitic brecciated tuff lavas (samples XRD111-1); (c) photomicrographs of the rhyolitic tuff lavas (sample KR570-4); (d) photomicrographs of the rhyolitic tuff lavas (sample KR570-5). Mineral abbreviations are as follows: Q = quartz, Or = K-feldspar, Pl = Plagioclase.

Rhyolitic tuff lava is light gray, light gray-green, and light gray-purple in color. The debris is mostly subangular and subrounded, sporadically scattered, with a grain size < 2 mm, occasionally 3 mm. The phenocrysts exist uniformly, and the minerals are distributed unevenly, mainly including quartz, K-feldspar, and plagioclase (Figure 4c). The crystals are angular to subangular with corrosion. Quartz is often corroded, with corrosion bays and perforations, accounting for 5–10% (Figure 4d). K-feldspar is mainly composed of orthoclase, accounting for 15%, and plagioclase is mainly composed of oligoclase and andesine, accounting for approximately 10%. There is a small amount of dark mineral, which has been strongly altered, and the particle size is ≤ 2 mm. The matrix is composed of lava, with scattered volcanic debris (debris, crystal) and phenocrysts. The matrix is fine-grained, with microcrystalline structure, local flow structure (rhyolite structure), and recrystallization can be seen locally. It is mainly composed of feldspar (main) and quartz (secondary), with a content of 65%. In addition, a small amount of secondary sericite and calcite and other minerals occur in the matrix.

4. Analytical Methods

4.1. LA-ICP-MS Testing

Zircon U-Pb dating was performed on rhyolitic brecciated tuff lavas (sample XRD110-5) and rhyolitic tuff lavas (sample XRD111-3) from the Keri rhyolites. The locations of the two samples are $36^{\circ} 00' 43.8''$ N, $97^{\circ} 41' 24.5''$ E, and $36^{\circ} 00' 30.2''$ N, $97^{\circ} 41' 09.1''$ E (Figure 2). The zircon age samples were pretreated at Fengzeyuan Rock and Mineral Testing Technology Co. The zircon was crushed by conventional methods, sorted by conventional flotation methods, and finally zircon with good crystal shape and transparency was selected as the dating object using binoculars. The zircon grains were mounted on double-faced adhesive tape, and after the epoxy resin fixation–epoxy resin curing–

surface polishing process, zircon micrographs and cathodoluminescence photograms were performed. Cathodoluminescence (CL) microphotographic images were taken with a Cameca electron probe X-ray microanalyzer at the Beijing Geoanalysis Co., Ltd (Beijing, China).

In situ U-Pb isotopic age analyses of zircons were performed using LA-ICP-MS at the Tianjin Geological Survey Center of China Geological Survey. The analysis instruments were Elan Geo-Las200M-Type Quadrupole Perch Mass Spectrograph equipped with an Elan6100 DRC excimer laser ablation system (193 nm, A Rf- excimer, Lambda Physic). The facula beam diameter for laser ablation was 30 μm , and the depth of laser ablation samples was 20 to 40 μm . The international zircon standard 91,500 was used as an external standard for the calculation of zircon ages. The artificial synthetic silicate glass NIST610, American National Standard Substance Bureau, was adopted as an external standard for element content analysis. ^{29}Si was used as the internal standard element. The isotopic ratio and element content data were analyzed using the ICPMS Data Cal software package [61]. The general lead adjustment was conducted using the Andersen software [62], and Isoplot software (3.0 edition) [63] was used for age calculation and concordia diagrams. The analytical methods and instrument settings used were the same as those reported by Li et al. [64].

4.2. Geochemical Analyses

Sixteen samples were selected for major and trace element analyses. The samples were ground to 200 mesh. Major and trace elements were measured in the Key Laboratory of Western China's Mineral Resources and Geological Engineering, Ministry of Education, Chang'an University. The major elements were measured with X-ray fluorescence spectrometry (XRF-1500). The detailed technical requirements and test process are from the references [4].

5. Results of Analyses

The zircon U-Pb isotope data and whole-rock geochemistry for the Keri rhyolites are listed in Supplementary Tables S1 and S2.

5.1. Zircon U-Pb Age

Zircons selected from the Keri rhyolites of the rhyolitic brecciated tuff lava (sample XRD110-5) and rhyolitic tuff lava (sample XRD111-3) are columnar euhedral to elliptical prismatic with light yellow–colorless transparent color and show obvious magmatic oscillatory zoning (Figure 5a,b), indicating a magmatic origin [65–67]. Zircon crystals have lengths ranging from 50 μm to 250 μm and length/width ratios ranging from 3:1 to 1:1. The Th content of sample XRD110-5 ranges from 220 to 477 ppm with U contents of 431–776 ppm, and with Th/U ratios from 0.51 to 0.67 (Supplementary Table S1). The Th/U ratio is greater than 0.4 (Figure 5c) and the Th and U are positively correlated (Figure 5d). The Th contents of sample XRD111-3 ranges from 178 to 683 ppm and U contents ranges 350–707 ppm, with Th/U ratios from 0.46 to 1.47 (Supplementary Table S1). The Th/U ratio is greater than 0.4 (Figure 5e). Th and U are positively correlated (Figure 5f). All Th/U ratios are higher than 0.4, and Th and U contents show a positive correlation, indicating a magmatic origin as well [68].

The $^{206}\text{Pb}/^{238}\text{U}$ and $^{207}\text{Pb}/^{235}\text{U}$ at 21 measurement points of the sample XRD110-5 have good concordance (Figure 5g). $^{206}\text{Pb}/^{238}\text{U}$ ages range from 197 ± 2 Ma to 208 ± 1 Ma (Supplementary Table S1), with a weighted mean age of 202.8 ± 1.2 Ma (MSWD = 1.15, Figure 5h), representing the crystallization age of the rhyolitic brecciated tuff lava.

The 21 measurement points $^{206}\text{Pb}/^{238}\text{U}$ and $^{207}\text{Pb}/^{235}\text{U}$ of the sample XRD111-3 have a general concordance (Figure 5i). The 14 effective measurement points have a good concordance (Figure 5j). The $^{206}\text{Pb}/^{238}\text{U}$ age ranges from 195 ± 4 Ma to 204 ± 2 Ma (Supplementary Table S1), with a weighted mean age of 200.4 ± 1.4 Ma (MSWD = 2.8, Figure 5k).

Therefore, the preferred crystallization age of the Keri rhyolite is 200.4–202.8 Ma, which was during in the Late Triassic Rhaetian to Early Jurassic Hettangian.

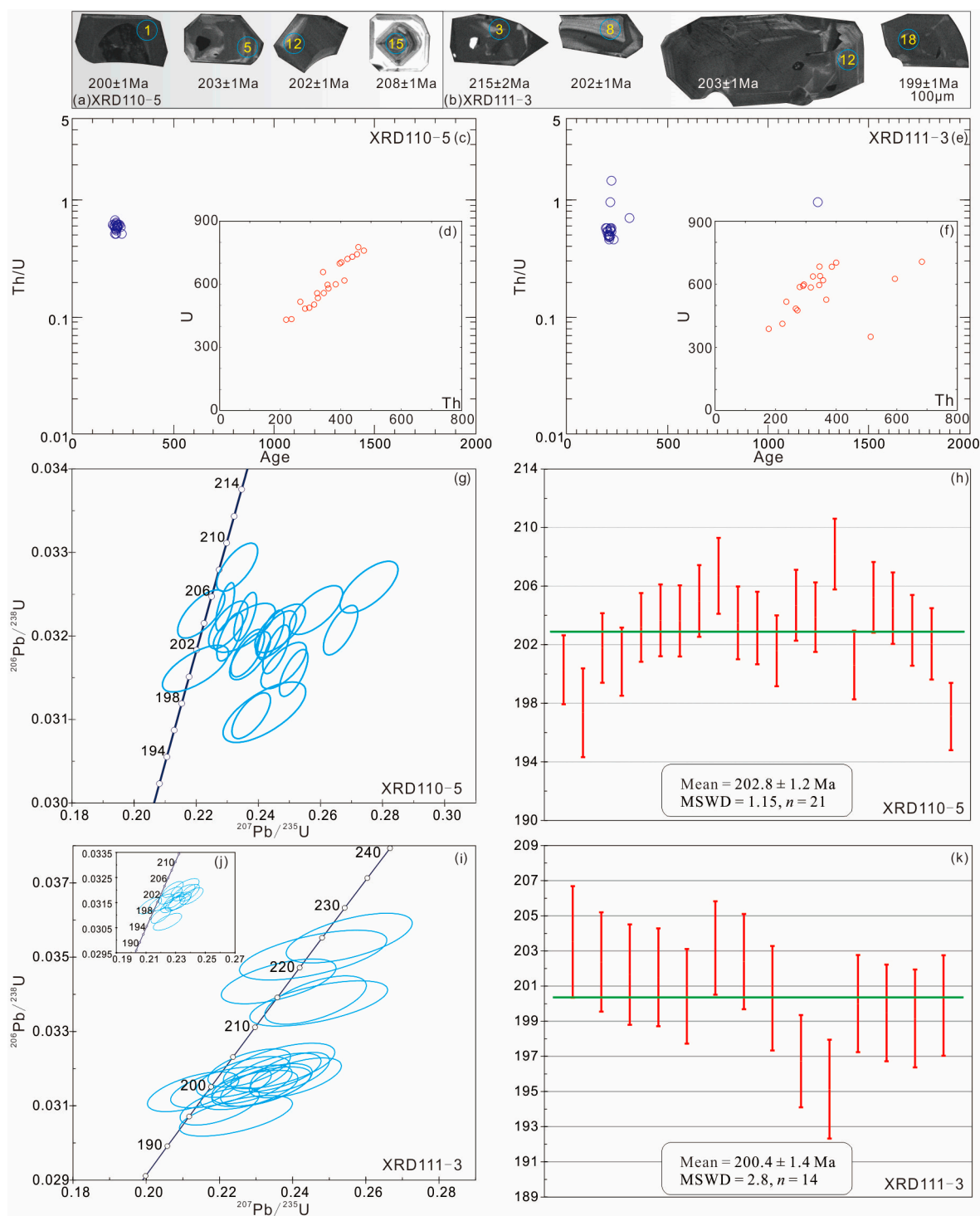


Figure 5. (a,b) CL images and single-zircon $^{206}\text{Pb}/^{238}\text{U}$ ages of zircons; (c) Th/U vs. age of zircon diagram of sample XRD110-5; (d) Th vs. U content of zircon diagram of sample XRD110-5; (e) Th/U vs. age of zircon diagram of sample XRD111-3; (f) Th vs. U content of zircon diagram of sample XRD111-3; (g,h) LA-ICP-MS zircon U-Pb concordia diagram of sample XRD110-5; (i-k) LA-ICP-MS zircon U-Pb concordia diagram of sample XRD111-3 of the Keri rhyolites in the EKOB.

5.2. Major and Trace Element Geochemistry

Major and trace element data and calculated parameters for 11 representative samples are listed in Supplementary Table S2. All samples exhibit relatively uniform major oxide compositions.

5.2.1. Major Elements

The SiO_2 contents of the Keri rhyolites ranges from 72.95 to 76.02 wt.% (Supplementary Table S2). In the total alkali versus silica classification diagram (Figure 6a), they all fall into the rhyolite area and the subalkaline series. The Keri rhyolites have Al_2O_3 contents ranges from 12.02 to 13.30 wt.%, MgO contents from 0.01 to 0.08 wt.%, CaO contents from 0.36 to 0.57 wt.%, Na_2O contents from 2.12 to 4.04 wt.%, with K_2O contents from 4.63 to 8.03 wt.%. In the K_2O versus SiO_2 diagram (Figure 6b), except for six samples falling into the shoshonite series, other samples plot within the high-K calc-alkaline series, with total alkali contents between 8.37 and 10.10 wt.%, $\text{K}_2\text{O}/\text{Na}_2\text{O}$ values between 1.19 and 3.88, the alkali rate (A.R.) ranging from 4.64 to 7.18, and the Rittmann index (σ) ranging from 2.12 to 3.39. In a $(\text{Na}_2\text{O} + \text{K}_2\text{O} - \text{CaO})$ versus SiO_2 diagram (Figure 6c), the samples plot in the boundary between alkalic and alkali-calcic and within the A-type granite area. In the A/NK-A/CNK diagram (Figure 6d), the samples plot in the weakly peraluminous fields with A/CNK ranging from 0.97 to 1.09 and low $\text{FeO}/(\text{FeO} + \text{MgO})$ ratios ranging from 0.96 to 1.00. In the Harker diagram (Figure 7), there is a good linear relationship between the major elements and SiO_2 in the Keri rhyolites and the Elashan Formation volcanic rocks.

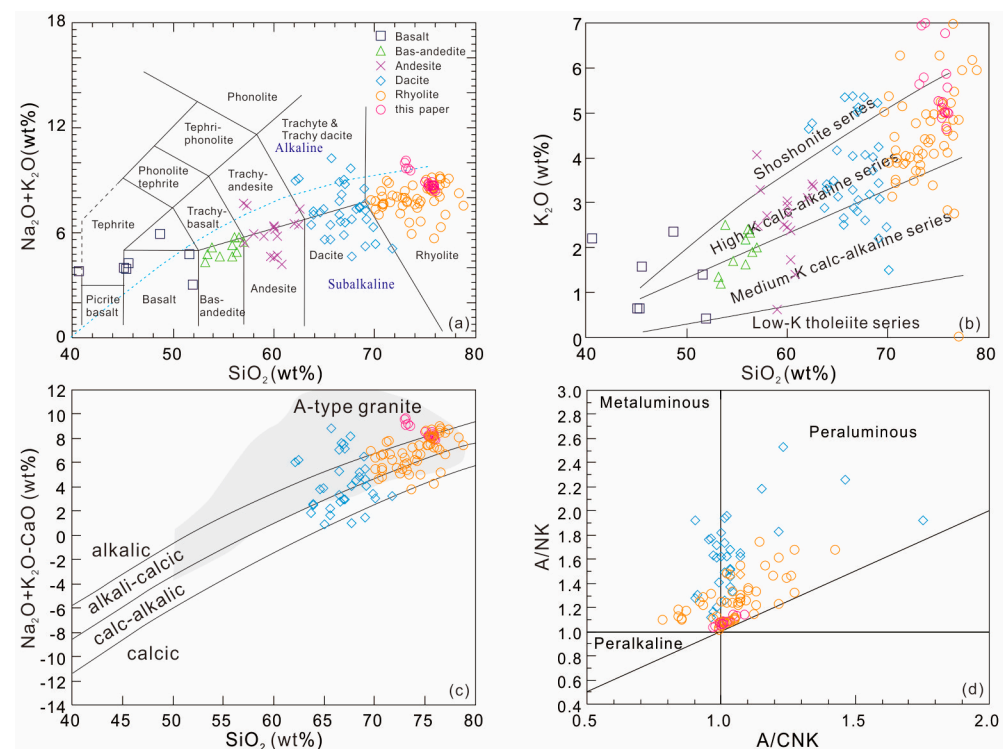


Figure 6. (a) TAS diagrams (after Middlemost [69]); (b) K_2O vs. SiO_2 diagrams (after Rickwood [70]); (c) $(\text{Na}_2\text{O} + \text{K}_2\text{O} - \text{CaO})$ vs. SiO_2 diagrams (after Frost et al. [71]); (d) A/NK vs. A/CNK diagrams (after Maniar et al. [72]) for the Keri rhyolites in the EKOB. Geochemical data of Elashan Formation volcanics from references [43–53].

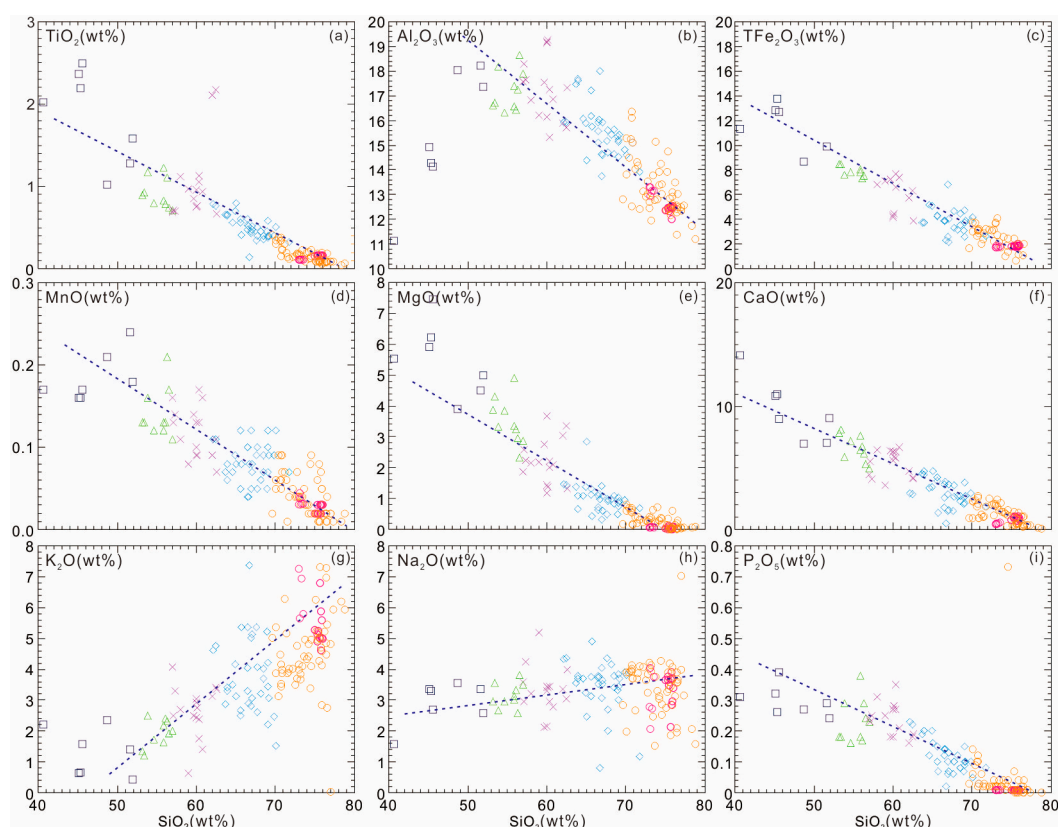


Figure 7. Harker diagrams of the Keri rhyolites in the EKOB. Dashed lines show linear trends, indicating the important role of magma mixing. (a) SiO_2 vs. TiO_2 diagram; (b) SiO_2 vs. Al_2O_3 diagram; (c) SiO_2 vs. TFe_2O_3 diagram; (d) SiO_2 vs. MnO diagram; (e) SiO_2 vs. MgO diagram; (f) SiO_2 vs. CaO diagram; (g) SiO_2 vs. K_2O diagram; (h) SiO_2 vs. Na_2O diagram; (i) SiO_2 vs. P_2O_5 diagram.

5.2.2. Rare Earth Elements

Trace element results indicate that the Keri rhyolites have low REE contents of 133.11 to 333.34 ppm (average of 211.10 ppm, Supplementary Table S2). The fractionation between LREE and HREE ranges from LREE/HREE ratios of 7.63 to 20.04, with $(\text{La}/\text{Yb})_{\text{N}}$ ratios ranging from 9.15 to 29.31, $\text{Eu}/\text{Eu}^* = 0.01\text{--}0.02$, and the LREE internal differentiation is 3.65–5.05, which is relatively obvious $(\text{La}/\text{Sm})_{\text{N}}$. In the chondrite-normalized REE distribution diagram for the Keri rhyolites (Figure 8a), as well as right-dipping seagull-type enrichment in LREE versus depletion in HREE [73], there is a significant negative Eu anomaly.

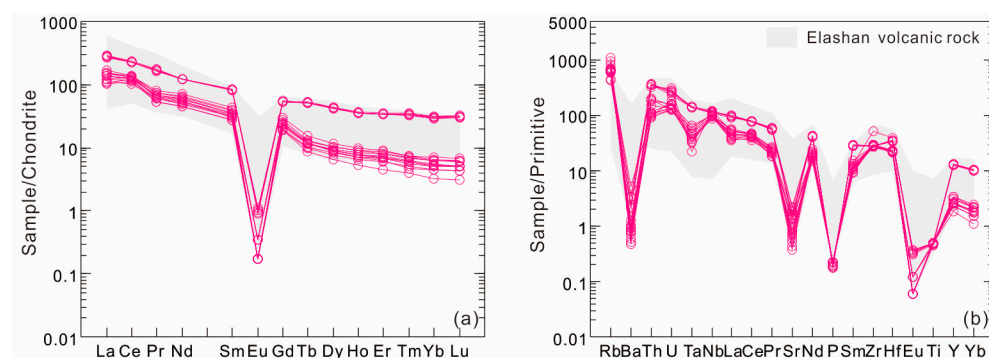


Figure 8. (a) Chondrite-normalized rare earth element (REE) patterns; (b) primitive-normalized incompatible element distribution patterns for the Keri rhyolites in the EKOB (chondrite data and primitive data for normalization taken from Sun et al. [73]). Geochemical data of Elashan Formation volcanics from references [43–53].

5.2.3. Trace Elements

On the primitive mantle-normalized spider diagram (Figure 8b), the Keri rhyolites are enriched in some high-field-strength elements (HFSE, such as Hf) and some large-ion lithophile elements (LILEs, such as Rb, Zr, Nd, Th, and U). Our samples are depleted in other HFSEs and LILEs, such as P, Ti, Eu, Sr, and Ba. The spider diagram curves and REE patterns among all samples are identical, representing their cognate source rocks.

6. Discussion

6.1. Age of Volcanic Rocks

The weighted mean ages of the Keri rhyolites are between 200.4 ± 1.4 Ma and 202.8 ± 1.2 Ma, which represents the formation age of the volcanic rocks formed in the Late Triassic Rhaetian–Early Jurassic Hettangian.

The zircon U–Pb ages of the Elashan Formation volcanic rocks in the region range from 231.9 to 208.4 Ma [47,48,52,53,74]. Based on the statistical analysis of the existing single grain zircon ages, we found that the $^{206}\text{Pb}/^{238}\text{U}$ ages of the Elashan Formation volcanic rocks range from 195 to 239 Ma, with two obvious peak ages at 227.62 Ma and 209.98 Ma, a small peak at 202.65 Ma, and an obvious valley at 215 to 220 Ma (Figure 9a). According to the further classification of sample lithology, it is found that the formation age of basalt ranges from 229–233 Ma, and the peak age appears at 230 Ma; The formation age of andesite ranges from 208–239 Ma, with the peak appearing at 230 Ma and 223–224 Ma; The formation age of rhyolite ranges from 195 Ma to 238 Ma, the peak value from 207 Ma to 212 Ma (Figure 9b). These data are consistent with the rock combination characteristics of the Elashan Formation. Therefore, the Elashan Formation volcanic rocks were mainly formed in the Late Triassic and may extend to the early Early Jurassic. They are characterized by the evolution of basic, intermediate, and acidic volcanic rocks. The magma has a certain genetic evolution relationship. The Keri rhyolite is a product of the late magmatism of the Elashan Formation volcanic rocks.

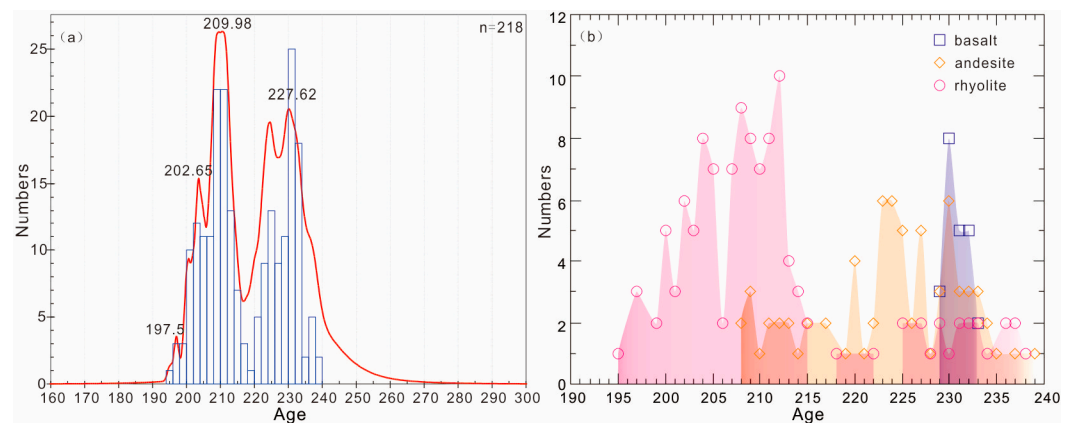


Figure 9. (a) Statistical analysis on the age; (b) Statistical analysis on the age of basalt, andesite and rhyolite of the Elashan Formation volcanic rocks in the northern margin of the EKOB (In subfigure (a), zircon age data from references [47,48,52,53]; this paper. In subfigure (b), basalt zircon age data from references [47]; andesite zircon age data from references [48,52,53]; rhyolite zircon age data from references [52,53]; this paper).

6.2. Rock Types

A-type magmatic rocks are characterized by alkaline, anhydrous, and anorogenic features [75], which were formed in a unique tectonic setting and are still used today. However, with the further study of A-type magmatic rocks, their characteristics have also changed correspondingly. For example, some A-type magmatic rocks are not anhydrous, and some A-type magmatic rocks show metaluminous and peraluminous characteristics

[76–78]. In addition, some A-type magmatic rocks may have formed in a post-orogenic environment [79–81].

The high SiO_2 content features high-evolution magmatic rock sequences, and A-type, S-type, and I-type of high-evolution magmatic rocks can show similar geochemical characteristics. Relatively speaking, the high-evolution S-type granite has a high P_2O_5 content (the average value of P_2O_5 is 0.14 wt.%, King et al. [82]), and the high-evolution I-type granite has a low TFe_2O_3 content (generally less than 1 wt.%, Jia et al., [83]). The Keri rhyolite is characterized by high SiO_2 , K_2O , alkali, TFe_2O_3 content (1.74–2.05 wt.%) and low P_2O_5 content (0.01 wt.%), showing the characteristics of A-type granite, which excludes the possibility that the Keri rhyolite belongs to the highly differentiated I-type and S-type magmatic rocks.

The Keri rhyolite 10,000Ga/Al ratio (10,000Ga/Al = 3.31–4.45, with an average value of 3.93) is > 2.6 , which is higher than the average value of I-type granite and S-type granite (2.10 and 2.28, respectively), and higher than the lower limit value of 2.60 of A-type granite [84]. High Zr, Nb, Ce, and Y content ($\text{Zr} + \text{Nb} + \text{Ce} + \text{Y} = 450.62\text{--}766.63 \text{ ppm} > 350 \text{ ppm}$) and TiO_2 content (0.10–0.11) [85], the chondrite-normalized REE distribution diagram shows a similar right-dipping seagull type, with obvious negative Eu anomaly (Figure 8a) [86], similar to typical A-type granite [84,87,88]. In the discrimination diagram [84], the Keri rhyolite samples all fall into the A-type magmatic rock area (Figure 10a,d). Therefore, the Keri rhyolite is an A-type rhyolite, which is consistent with the characteristics of the A-type magmatic rocks of most of the intermediate acidic volcanic rocks of the Elashan Formation.

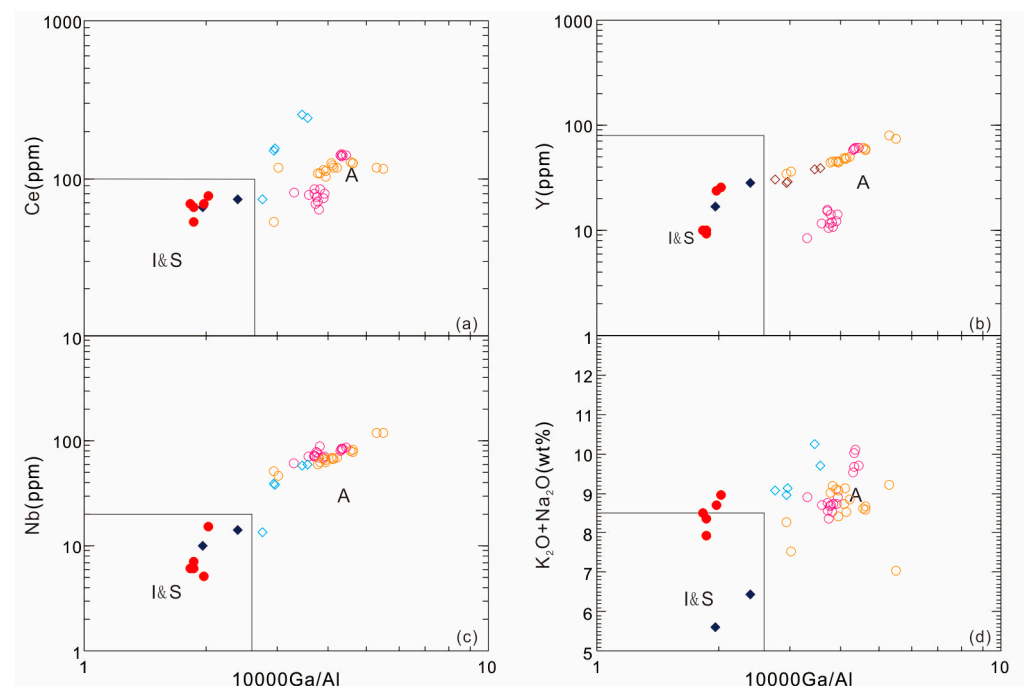


Figure 10. Ce (a), Y (b), Nb (c), and $(\text{K}_2\text{O} + \text{Na}_2\text{O})$ (d) vs. 10,000 Ga/Al discrimination diagrams for the Keri rhyolite in the EKOB (after Whalen et al. [84]). A = A-type granitoids; I = I-type granitoids; S = S-type granitoids.

6.3. Petrogenesis

At present, there are three main views on the formation mechanism of A-type magmatic rocks: crystallization differentiation of mantle derived magma [80,89–91], mixing of mantle-derived magma and crust-derived magma [91–93], and partial melting of crustal materials [89,94–97].

The crystallization differentiation of mantle-derived basaltic melts usually produces peralkaline magma [82,94], which is inconsistent with the peraluminous characteristic of

the Keri rhyolite (Figure 6d). The Keri rhyolite has lower Cr (0.39–30.64 ppm) and Ni (0.30–37.57 ppm) contents, which are closer to crustal source (the contents of Cr and Ni in the crust are approximately 5.00–33.0 ppm and 3.00–39.0 ppm, respectively; Lara et al. [98]). On the other hand, the Th/U value of the volcanic rock ranges from 2.12 to 6.21 (average value is 4.40); the value of Nb/Ta ranges from 14.16 to 94.92 (average value is 35.07), showing the characteristics of crust–mantle mixing (Th/U value of lower crust ranges from 3.80–6.00, Th/U value of primitive mantle is 4.00, Nb/Ta value of mantle-derived magma is 17.5 ± 2 , Nb/Ta value of crust-derived magma is 11.0–12.0; Gao et al. [99]). In the TFe_2O_3 –MgO diagram (Figure 11a), the Keri rhyolite has a certain evolutionary relationship with the samples of the Elashan Formation in the region, falling on the curve of the magma mixing trend, reflecting that they had undergone chemical mixing [100–102].

Research shows that A-type magmatic rocks can be partially melted from felsic magmatic rocks under high temperature and a low-pressure environment [103–105], and A-type magmatic rocks formed in this environment have metaluminous–weak peraluminous characteristics [71,94,103,106]. The A/CNK value of the Keri rhyolite ranges from 0.97 to 1.09, and are weakly peraluminous in character, suggesting a crustal origin [107], which is consistent with the metaluminous–weak peraluminous A-type granite formed in a high-temperature and low-pressure environment. The Rb/Sr ratio ranges from 8.31 to 51.85 (average 22.84), the Ti/Y ratio ranges from 10.42 to 77.97 (average 40.55), and the Ti/Zr ratio ranges from 1.13 to 2.16 (average 1.96) are in the range of crustal magma ($\text{Rb/Sr} > 0.5$, $\text{Ti/Y} < 100$, $\text{Ti/Zr} < 20$) [108–110], indicating a crustal origin of the magma. At the same time, the low $\epsilon_{\text{Nd}}(t)$ value of -2.6 – -2.5 and $\epsilon_{\text{Hf}}(t)$ value ranges from -2.8 to 2.9 for the rhyolite in the neighboring area [53] similarly shows a crustal origin. On Th/Yb versus Ta/Yb (Figure 11b), the samples are all located near the crustal area.

The Keri rhyolites have spherulite textures, which are mainly composed of quartz and alkali feldspar. The spherulite cores are more numerous, and the cores are commonly crystal nucleus, similar to those formed by rapid condensation, which are different from those formed by devitrification. The REE distribution pattern is almost identical to the trace element spider diagram (Figure 8), indicating the same magma source.

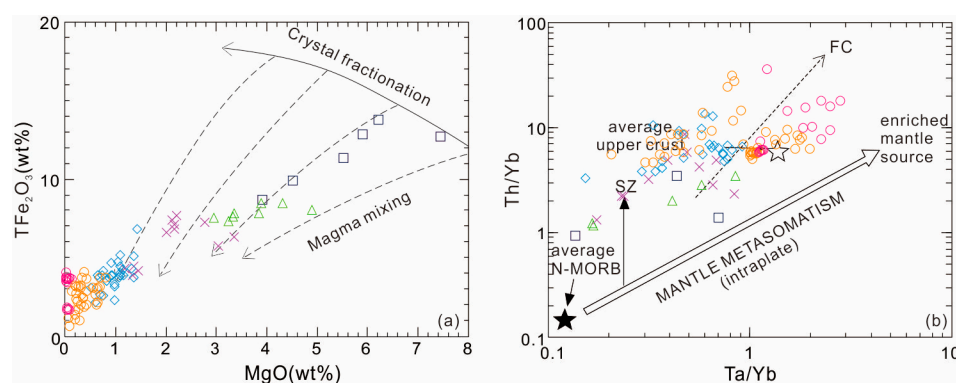


Figure 11. (a) TFe_2O_3 vs. MgO diagrams (after Zorpi et al. [111]); (b) Th/Yb vs. Ta/Yb diagrams (after Jahn et al. [112]). The compositions of the MORB (mid-ocean ridge basalt), and upper crusts are after Taylor et al. [113]; the vectors for intra-plate enrichment are based on the data of Pearce et al. [114]).

In summary, the Keri A-type rhyolite is concluded to have formed by mixing crust-derived magma with a small amount of mantle-derived magma. The magma source area would be mainly young crustal melt of Mesoproterozoic accretion and mixed with a small amount of mantle-derived magma. Its magma evolution process was mainly controlled by partial melting.

6.4. Tectonic Setting

From the field geology, the Elashan Formation is unconformable with the underlying strata and/or a set of volcanoclastic rocks above the intrusion [42], which is mainly

composed of volcanic lava and unstable sedimentary clastic rocks, without being deformed itself, and its distribution direction is not bounded by the regional tectonic boundaries, indicating that the Elashan Formation volcanic rocks were first formed after the post-collision stage and the regional tectonic deformation.

From the viewpoint of rock assemblage, the lower layer of the Elashan Formation is dominated by intermediate–basic volcanic rocks interspersed with clastic rocks. The middle layer is medium-acidic gray green dacite lava tuff; the upper layer is dominated by acidic volcanic rocks mixed with clastic rocks, with more lava and continental eruption characteristics. In general, it is a set of volcanic rocks that has evolved continuously from basic volcanic rocks to intermediate acidic volcanic rocks, and from calc-alkaline series to high-K calc-alkaline series. It is obviously different from island arc environment volcanic rocks dominated by basalt–andesite of low-K tholeiite series and is similar to the active continental margin environment volcanic assemblage. On the tectonic discrimination diagram (Figure 12a–d), Keri rhyolite samples all fall into the intraplate granite (WPG) and volcanic arc or late and post-collision areas.

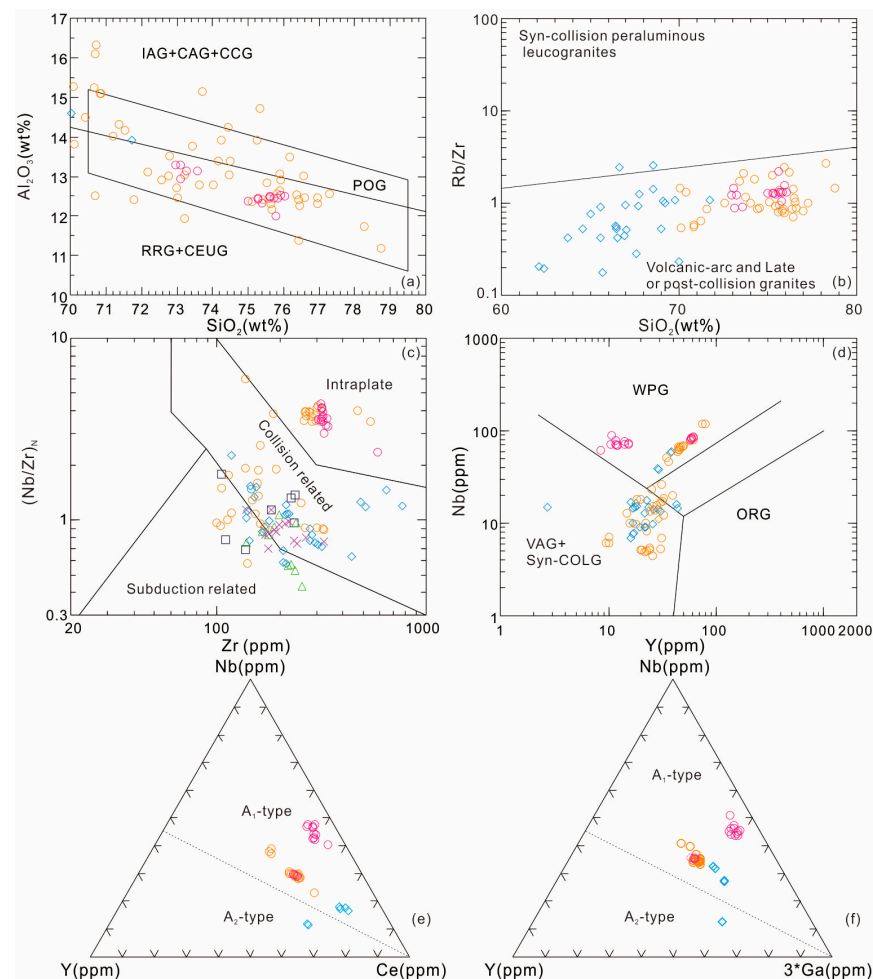


Figure 12. Diagrams of the tectonic settings of the Keri rhyolites in the EKOB. (a) after Maniar et al. [72]; (b) after Harris et al. [115]; (c) after Thieblemont et al. [116]; (d) after Pearce et al. [86]; (e,f) after Eby [80]. VAG = volcanic arc granites; Syn-COLG = syn-collision granites; WPG = within-plate granites; ORG = ocean ridge granites; Post-COLG = post-collision granites; MORB = mid-ocean ridge basalt; OIB = oceanic island basalts; WPB = within-plate basalts; IAB = island-arc tholeiites; MORB = mid-ocean ridge basalts; IAG = island arc granitoids; CAG = continental arc granitoids; CCG = continental collision granitoids; POG = post-orogenic granitoids; RRG = rift-related granitoids; CEUG = continental epeirogenic uplift granitoids. A₁-type = anorogenic environment; A₂-type = post-orogenic environment.

From geochemistry, the Keri rhyolite is a weakly peraluminous, high-K calc alkaline A-type rhyolite with high SiO_2 , $\text{K}_2\text{O}/\text{Na}_2\text{O}$, and A-type granite that is usually produced in an extensional tectonic environment [79,83,87,94,117–119]. The Y/Nb value of Keri rhyolite ranges from 0.12 to 0.73, with an average of 0.34 (less than 1.2), which conforms to the chemical classification of A₁-type granite. On the tectonic environment discrimination diagrams Nb–Y–Ga and Nb–Y–Ce (Figure 12e,f), the samples are all located in the A₁-type anorogenic environment area. This indicates that the rhyolite was formed in an intraplate anorogenic tectonic setting [80,86,87].

In conclusion, according to the field characteristics, geochemical characteristics, and the high formation temperature of the Keri rhyolite, it is speculated that the Keri rhyolite is a product of dehydration melting of calc-alkaline magmas in the shallow crust, formed in an anorogenic high-temperature and low-pressure environment, with intraplate genetic characteristics.

6.5. Tectonic Significance

Due to the subduction of Buqingshan–A'nyemaqen Ocean on the southern margin of the East Kunlun, a large number of arc magmatic rocks with metaluminous, medium-K calc alkaline characteristics were formed in the East Kunlun area during 260–240 Ma [3–6, 13,15–17,20–26,29,30,37,38,120–129]. With the collision between the Bayan Hara block and the East Kunlun block, the intrusive rocks in the East Kunlun area were rarely exposed during 240–230 Ma, and entered a period of magmatic quiescence [4,18,19,119,127]. The Late Triassic magmatic rocks in the EKOB are close to the peraluminous high-K calc-alkaline series with post-collisional magmatism characteristics [130,131]. Some of the Late Triassic magmatic rocks have A-type granite characteristics, and the stitching plutons of the Gerizhuotuo diorite (225.8 ± 1.5 Ma) [132] exposed in the Buqingshan–A'nyemaqen Tectonic Mélange Belt and the Binggou basic dyke group (226 Ma) [133] in the East Kunlun area are representative magmatic rocks, indicating that since the Late Triassic, the tectonic system of the East Kunlun has changed from a compressional environment to an extensional environment [4,15–19,21,24,74,125,127,134–137].

The Late Triassic Elashan Formation exposed on the northern margin of the EKOB is a set of basic–intermediate–acidic volcanic rocks. It can be seen from the Harker diagram (Figure 7) that the major elements have a good linear relationship, indicating a possible comagmatic evolution. From the isotopic data, trachyandesite, andesite, and rhyolite in the Balong area have similar $(^{87}\text{Sr}/^{86}\text{Sr})_{i, \text{END}}(t)$ and T_{DM2} values [53], which also indicates a possible comagmatic evolutionary relationship. The Elashan Formation is unconformable with the underlying strata and/or intrusions. The facies distribution is not constrained by regional tectonic lines, indicating that it formed after collisional orogeny. The geochemical characteristics also show that the Elashan Formation volcanic rocks are characterized by the evolution of subduction–collision–intraplate volcanic rocks (Figure 12c). The rhyolite includes I or S type magmatic rocks and A-type magmatic rocks (Figure 10), of which the A-type magmatic rocks mostly have A₁-type characteristics. The formation age of basic–intermediate–acidic volcanic rocks also characteristics by continuous evolution. The early basic rocks may have a certain genetic evolution relationship with other magmas. The Keri rhyolite is a product of the late magmatism of the volcanic rocks of the Elashan Formation (Figure 13).

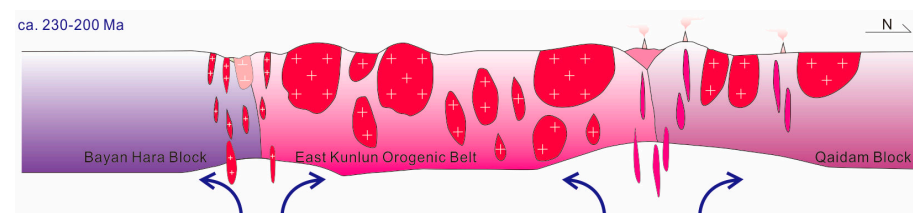


Figure 13. Tectonic evolution of the EKOB in Late Triassic.

7. Conclusions

From a comprehensive study of the Keri rhyolites in the EKOB based on petrological, geochronological, and geochemical analysis, we conclude the following.

- (1) The LA-ICP-MS zircon ages of the Keri rhyolites are between 200.4 ± 1.4 Ma and 202.8 ± 1.2 Ma, indicating that the volcanic rocks were formed in the Late Triassic Rhaetian–Early Jurassic Hettangian. The Keri rhyolite is a product of the late magmatism of the Elashan Formation volcanic rocks.
- (2) The Keri rhyolites have high SiO_2 , K_2O , alkali, TFe_2O_3 , and medium P_2O_5 contents and belong to peraluminous and the high-K calc-alkaline series, with significant negative Eu anomaly in the chondrite-normalized REE distribution diagram, as well as right-dipping seagull-type enrichment.
- (3) The Keri rhyolite, with the characteristics of A_1 -type magmatic rock, was formed in an anorogenic environment after the closure of the Paleo-Tethys Ocean and is a product of late magmatism in the Elashan Formation volcanic rocks.

Supplementary Materials: The following supporting information can be downloaded at: <https://www.mdpi.com/article/10.3390/min13020290/s1>, Table S1: Zircon LA-ICP-MS U-Pb data of the Keri rhyolites in the EKOB; Table S2: Whole-rock major and trace element data of the Keri rhyolites in the EKOB.

Author Contributions: Conceptualization, Z.L. and X.P.; methodology, Z.L. and S.Z.; software, L.P., L.Q., M.W. (Meng Wang), M.W. (Mao Wang) and L.X.; validation, Z.L., X.P. and C.L.; formal analysis, Z.L., X.P. and R.L.; investigation, Z.L., X.P., L.P., C.L., L.X., H.L., S.J. and Y.C.; resources, Z.L. and X.P.; data curation, Z.L. and X.P.; writing—original draft preparation, Z.L. and X.P.; writing—review and editing, Z.L., X.P. and Y.Y.; visualization, Z.L.; supervision, Z.L. and X.P.; project administration, Z.L. and X.P.; funding acquisition, Z.L. and X.P. All authors have read and agreed to the published version of the manuscript.

Funding: This research was funded by the National Nature Sciences Foundation of China (Grant Nos. 41872235, 42172236, 41802234, 41502191), Natural Science Basic Research Plan in Shaanxi Province of China (Grant Nos. 2019JM-312, 2019JQ-090, 2019JQ-209, 2020JM-229), the Fundamental Research Funds for the Central Universities (Grant Nos. 300102270202, 300103183081, 300103120009, 300104282717, 300102279204, 201810710233), China Scholarship Council (Grant No. 201806565026), the Commonweal Geological Survey, the Aluminum Corporation of China and the Land-Resources Department of Qinghai Province (Grant No. 200801), and the Youth Innovation Team of Shaanxi Universities.

Data Availability Statement: The original contributions presented in the study are included in the article/Supplementary Material.

Acknowledgments: Our thanks are extended to the chief editor and the four anonymous reviewers for their constructive reviews which have greatly improved our manuscript.

Conflicts of Interest: The authors declare no conflicts of interest.

References

1. Li, R.S.; Ji, W.H.; Pan, X.P. *Geological Map of Kunlun Mountains and Adjacent Areas (1:1,000,000)*; Geological Publishing House: Beijing, China, 2009. (In Chinese)
2. Luo, Z.H.; Ke, S.; Cao, Y.Q.; Deng, J.F.; Chen, H.W. Late Indosinian mantle-derived magmatism in the East Kunlun. *Geol. Bull. China* **2002**, *21*, 292–297. (In Chinese with English Abstract)
3. Mo, X.X.; Luo, Z.H.; Deng, J.F.; Yu, X.H.; Liu, C.D.; Chen, H.W.; Yuan, W.M.; Liu, Y.H. Granitoids and crustal growth in the East-Kunlun orogenic belt. *J. China Univ. Geosci.* **2007**, *13*, 403–414. (In Chinese with English Abstract)
4. Li, Z.C.; Pei, X.Z.; Bons, P.D.; Li, R.B.; Pei, L.; Chen, G.C.; Chen, Y.X.; Liu, C.J.; Wang, M.; Zhao, S.W.; et al. Petrogenesis and tectonic setting of the Early-Middle Triassic subduction-related granite in the eastern segment of East Kunlun: Evidences from petrology, geochemistry, and zircon U-Pb-Hf isotopes. *Int. Geol. Rev.* **2022**, *64*, 698–721.
5. Wang, H.Z. On the Geotectonic Units of Xizang (Tibet) Region. *Earth Sci.* **1983**, *19*, 1–8. (In Chinese with English Abstract)
6. Jiang, C.F.; Wang, Z.Q.; Li, J.Y. *Central Orogenic Belt in China*; Geological Publishing House: Beijing, China, 2000; pp. 154. (In Chinese with English Abstract)
7. Zhang, G.W.; Dong, Y.P.; Lai, S.C.; Guo, A.L.; Meng, Q.R.; Liu, S.F.; Cheng, S.Y.; Yao, A.P.; Zhang, Z.Q.; Pei, X.Z.; et al. Mianlüe tectonic zone and Mianlüe suture zone on southern margin of Qinling-Dabie orogenic belt. *Sci. China Ser. D* **2004**, *47*, 300–316.

8. Dong, Y.P.; He, D.F.; Sun, S.S.; Liu, X.M.; Zhou, X.H.; Zhang, F.F.; Yang, Z.; Cheng, B.; Zhao, G.C.; Li, J.H. Subduction and accretionary tectonics of the East Kunlun orogen, western segment of the Central China Orogenic System. *Earth-Sci. Rev.* **2018**, *186*, 231–261.
9. Liu, C.D.; Mo, X.X.; Luo, Z.H.; Yu, X.H.; Chen, H.W.; Li, S.W.; Zhao, X. Mixing events between the crust- and mantle-derived magmas in Eastern Kunlun: Evidence from zircon SHRIMP II chronology. *Chin. Sci. Bull.* **2004**, *49*, 828–834.
10. Liu, C.D. *Granite Magma Mixing in the Eastern Part of the Eastern Kunlun Orogenic Belt*; Geological Publishing House: Beijing, China, 2008; pp. 1–142. (In Chinese)
11. Mo, X.X.; Zhao, Z.D.; Deng, J.F.; Dong, G.C.; Zhou, S.; Guo, T.Y.; Zhang, S.Q.; Wang, L.L. Response of volcanism to the India-Asia collision. *Earth Sci. Front.* **2003**, *10*, 135–148. (In Chinese with English Abstract)
12. Liu, C.D.; Mo, X.X.; Luo, Z.H.; Yu, X.H.; Chen, H.W.; Li, S.W.; Zhao, X. Pb-Sr-Nd-O isotope characteristics of granitoids in East Kunlun orogenic belt. *Acta Geol. Sin.* **2003**, *24*, 584–588. (In Chinese with English Abstract)
13. Li, B.L.; Sun, F.Y.; Yu, X.F.; Qian, Y.; Wang, G.; Yang, Y.Q. U-Pb Dating and Geochemistry of Diorite in the Eastern Section from Eastern Kunlun Middle Uplifted Basement and Granitic Belt. *Acta Petrol. Sin.* **2012**, *28*, 1163–1172. (In Chinese with English Abstract)
14. Xu, Z.Q.; Yang, J.S.; Li, W.C.; Li, H.Q.; Cai, Z.H.; Yan, Z.; Ma, C.Q. Paleo-Tethys System and Accretionary Orogen in the Tiber Plateau. *Acta Petrol. Sin.* **2013**, *29*, 1847–1860. (In Chinese with English Abstract)
15. Chen, G.C.; Pei, X.Z.; Li, R.B.; Li, Z.C.; Pei, L.; Liu, Z.Q.; Chen, Y.X.; Liu, C.J.; Gao, J.M.; Wei, F.H. Zircon U-Pb geochronology, geochemical characteristics and geological significance of Cocoe A'Long quartz diorites body from the Hongshuichuan area in East Kunlun. *Acta Geol. Sin.* **2013**, *87*, 178–196. (In Chinese with English Abstract)
16. Chen, G.C.; Pei, X.Z.; Li, R.B.; Li, Z.C.; Pei, L.; Liu, Z.Q.; Chen, Y.X.; Liu, C.J. Late Triassic magma mixing in the East Kunlun orogenic belt: A case study of Helegang Xilikete granodiorites. *Geol. China* **2013**, *40*, 1044–1065. (In Chinese with English Abstract)
17. Chen, G.C.; Pei, X.Z.; Li, R.B.; Li, Z.C.; Pei, L.; Liu, Z.Q.; Chen, Y.X.; Liu, C.J.; Gao, J.M.; Wei, F.H. Geochronology and genesis of the Helegang Xilikete granitic plutons from the southern margin of the eastern East Kunlun orogenic belt and their tectonic significance. *Acta Geol. Sin.* **2013**, *87*, 1525–1541. (In Chinese with English Abstract)
18. Xia, R.; Wang, C.S.; Deng, J.; Carranza, E.J.M.; Li, W.L.; Qing, M. Crustal thickening prior to 220 Ma in the East Kunlun orogenic belt: Insights from the Late Triassic granitoids in the Xiao-Nuomuhong pluton. *J. Asian Earth Sci.* **2014**, *93*, 193–210.
19. Xiong, F.H.; Ma, C.Q.; Zhang, J.Y.; Liu, B.; Jiang, H.A. Reworking of old continental Lithosphere: An important crustal evolution mechanism in orogenic belts, as evidenced by Triassic I-type granitoids in the East Kunlun orogen, northern Tibetan Plateau. *J. Geol. Soc. Lond.* **2014**, *171*, 847–863.
20. Chen, G.; Pei, X.Z.; Li, Z.C.; Li, R.B.; Chen, Y.X.; Liu, C.J.; Chen, G.C.; Wang, X.B.; Sang, J.Z.; Yang, S.; et al. Zircon U-Pb geochronology, geochemical characteristics and geological significance of Chaohuolutaolegai granodiorite in Balong area, East Kunlun Mountains. *Geol. Bull. China* **2016**, *35*, 1990–2005. (In Chinese with English Abstract)
21. Hu, Y.; Niu, Y.L.; Li, J.Y.; Ye, L.; Kong, J.J.; Chen, S.; Zhang, Y.; Zhang, G.R. Petrogenesis and tectonic significance of the late Triassic mafic dikes and felsic volcanic rocks in the East Kunlun orogenic belt, northern Tibet Plateau. *Lithos* **2016**, *245*, 205–222.
22. Chen, G.C.; Pei, X.Z.; Li, R.B.; Li, Z.C.; Liu, C.J.; Chen, Y.X.; Pei, L.; Zhang, Y.M.; Wang, M.; Li, X.B.; et al. Age and petrogenesis of Jialuhe basic-intermediate pluton in Xiangjiananshan granite batholith in the eastern part of East Kunlun orogenic belt, and its geological significance. *Geotect. Metallog.* **2017**, *41*, 1097–1115. (In Chinese with English Abstract)
23. Chen, G.C.; Pei, X.Z.; Li, R.B.; Li, Z.C.; Pei, L.; Liu, C.J.; Chen, Y.X.; Li, X.B. Triassic magma mixing and mingling at the eastern section of Eastern Kunlun: A case study from Xiangjiananshan granitic batholith. *Acta Petrol. Sin.* **2018**, *34*, 2441–2480. (In Chinese with English Abstract)
24. Chen, G.C.; Pei, X.Z.; Li, R.B.; Li, Z.C.; Liu, C.J.; Chen, Y.X.; Pei, L.; Li, X.B. Age and lithogenesis of Keri syenogranite from eastern part of East Kunlun Orogenic Belt: Constraint on the middle triassic tectonic evolution of East Kunlun. *Acta Petrol. Sin.* **2018**, *343*, 567–585. (In Chinese with English Abstract)
25. Chen, G.C.; Pei, X.Z.; Li, R.B.; Li, Z.C.; Pei, L.; Liu, C.J.; Chen, Y.X.; Wang, M.; Zhang, Y.; Li, X.B. Magma mixing in Halagatu granitic batholith from eastern part of the East Kunlun orogenic belt: Constraints from lithology and mineralogy. *Earth Sci.* **2018**, *43*, 3200–3217. (In Chinese with English Abstract)
26. Hu, C.G.; Pei, X.Z.; Li, R.B.; Chen, Y.X.; Liu, C.J.; Li, Z.C.; Zhang, Y.; Yan, Q.Z.; Wang, X.; Peng, S.Z. Zircon U-Pb ages and geological significance of metamorphic basic intrusive rocks in the Acitearea of East Kunlun. *Northwestern Geol.* **2017**, *50*, 182–197. (In Chinese with English Abstract)
27. Liu, B.; Ma, C.Q.; Huang, J.; Wang, L.X.; Zhao, S.Q.; Yan, R.; Sun, Y.; Xiong, F.H. Petrogenesis and tectonic implications of Upper Triassic appinite dykes in the East Kunlun orogenic belt, northern Tibetan Plateau. *Lithos* **2017**, *284–285*, 766–778.
28. Shao, F.L.; Niu, Y.L.; Liu, Y.; Chen, S.; Kong, J.J.; Duan, M. Petrogenesis of Triassic granitoids in the East Kunlun orogenic belt, northern Tibetan Plateau and their tectonic implications. *Lithos* **2017**, *282–283*, 33–44.
29. Zhang, Y.; Pei, X.Z.; Li, R.B.; Liu, C.J.; Chen, Y.X.; Li, Z.C.; Wang, X.; Hu, C.G.; Yan, Q.Z.; Peng, S.Z. Zircon U-Pb geochronology, geochemistry of the Alasimu gabbro in eastern section of East Kunlun mountains and the closing time of Paleo-ocean basin. *Geol. China* **2017**, *44*, 526–540. (In Chinese with English Abstract)
30. Li, R.B.; Pei, X.Z.; Li, Z.C.; Pei, L.; Chen, G.C.; Chen, Y.X.; Liu, C.J.; Wang, S.M. Paleo-Tethys Ocean subduction in eastern section of East Kunlun Orogen: Evidence from the geochronology and geochemistry of the Wutuo pluton. *Acta Petrol. Sin.* **2018**, *3411*, 3399–3421. (In Chinese with English Abstract)

31. Pei, X.Z.; Li, R.B.; Li, Z.C.; Liu, C.J.; Chen, Y.X.; Pei, L.; Liu, Z.Q.; Chen, G.C.; Li, X.B.; Wang, M. Composition feature and formation process of Buqingshan composite accretionary mélangé belt in southern margin of East Kunlun orogen. *Earth Sci.* **2018**, *43*, 4498–4520. (In Chinese with English Abstract)
32. Xiong, F.H.; Ma, C.Q.; Chen, B.; Ducea, M.N.; Hou, M.C.; Ni, S.J. Intermediate-mafic dikes in the East Kunlun Orogen, Northern Tibetan Plateau: A window into Paleo-arc magma feeding system. *Lithos* **2019**, *340–341*, 152–165.
33. Xiong, F.H.; Meng, Y.K.; Yang, J.S.; Liu, Z.; Xu, X.Z.; Eslami, A.; Zhang, R. Geochronology and petrogenesis of the mafic dykes from the Purang ophiolite: Implications for evolution of the western Yarlung-Tsangpo suture zone, southwestern Tibet. *Geosci. Front.* **2020**, *11*, 277–292.
34. Yu, M.; Dick, J.M.; Feng, C.Y.; Li, B.; Wang, H. The tectonic evolution of the East Kunlun Orogen, northern Tibetan Plateau: A critical review with an integrated geodynamic model. *J. Asian Earth Sci.* **2020**, *191*, 104168.
35. Zhao, X.; Wei, J.H.; Fu, L.B.; Huizenga, J.M.; Santosh, M.; Chen, J.J.; Wang, D.Z.; Li, A.B. Multi-stage crustal melting from Late Permian back-arc extension through Middle Triassic continental collision to Late Triassic post-collisional extension in the East Kunlun Orogen. *Lithos* **2020**, *360–361*, 105446.
36. Kamaunji, V.D.; Wang, L.X.; Ma, C.Q.; Liu, J.; Zhu, Y.X. Petrogenesis and tectonic implication of the Permian-Triassic syenogranites from the eastern segment of the East Kunlun Orogen, China. *Lithos* **2021**, *402–403*, 105932.
37. Chen, G.C.; Pei, X.Z.; Li, R.B.; Li, Z.C.; Chen, Y.X.; Liu, C.J.; Pei, L. Multiple Sources of Indosinian Granites and Constraints on the Tectonic Evolution of the Paleo-Tethys Ocean in East Kunlun Orogen. *Minerals* **2022**, *12*, 1604.
38. Chen, X.D.; Li, B.; Yu, M.; Zhang, W.D.; Zhu, L. Generation of crystal-rich rhyodacites by fluid-induced crystal-mush rejuvenation: Perspective from the Late Triassic Nageng (sub-) volcanic complex of the East Kunlun Orogen, NW China. *Chem. Geol.* **2022**, *599*, 120833.
39. Li, R.B.; Pei, X.Z.; Li, Z.C.; Pei, L.; Chen, G.C.; Liu, Z.Q.; Chen, Y.X.; Liu, C.J.; Wang, M.; Zhang, M. Paleo-Tethys Ocean Evolution and Indosinian Orogenesis in the East Kunlun Orogen, Northern Tibetan Plateau. *Minerals* **2022**, *12*, 1590.
40. Xing, L.; Li, W.C.; Liu, J.; Zang, M.; Yang, F.C.; Liu, H.; Liu, W.G.; Guo, L.; Liu, B. Mineralization timing and genesis of the Qukulekedong Au-Sb deposit in the East Kunlun Orogenic Belt, northern Tibetan Plateau: Constraints from arsenopyrite Re-Os ages, zircon U-Pb ages, and Lu-Hf isotopes. *Ore Geol. Rev.* **2022**, *143*, 104731.
41. Feng, D.; Wang, C.; Song, S.G.; Xiong, L.; Zhang, G.B.; Allen, M.B.; Dong, J.; Wen, T.; Su, L. Tracing tectonic processes from Proto- to Paleo-Tethys in the East Kunlun Orogen by detrital zircons. *Gondwana Res.* **2023**, *115*, 1–16.
42. Bureau of Geology and Mineral Resources of Qinghai Province. *Stratigraphy (Lithostratic) of Qinghai Province*; China University of Geosciences Press: Wuhan, China, 1997; pp. 1–340. (In Chinese with English Abstract)
43. Tong, H.K.; Wang, S.L.; Song, S.C.; Tan, S.X.; Ma, X.L.; Huang, Q.H. Study on volcanic rocks and their structural environment of Late Triassic Epoch in Chachaxiangka area in Qinghai Province. *Earthq. Res. Plateau* **2004**, *16*, 38–48. (In Chinese with English Abstract)
44. Xia, C.L.; Ren, E.F.; Gao, L.; Zhou, S.M. Analysis of the geological features and tectonic setting of volcanic lava in Elashan group, Qinghai Province. *J. Qinghai Univ. (Nature Sci.)* **2011**, *29*, 48–53. (In Chinese with English Abstract)
45. Li, Y.D.; Liu, X.Y. Geochemistry and Tectonic Setting of Late Triassic Volcanic Rocks in Reshui Area, Qinghai. *Northwestern Geol.* **2014**, *47*, 14–25. (In Chinese with English Abstract)
46. Ma, Z.Y.; Ma, C.X.; Ye, Z.F.; Hao, Y.; Ma, F.S.; Tong, M.H.; Zhou, Q.L. Rock and geochemical characteristics of late Triassic continental volcanic rock of Elashan group in the East Kunlun. *J. Qinghai Univ.* **2016**, *34*, 31–37. (In Chinese with English Abstract)
47. Zhang, D.X.; Zeng, X.P.; Wei, X.L.; Wei, Y.X.; Yang, Y.Q.; Li, J.T. Geochemistry and Tectonic Setting of Late Triassic Volcanics in Elashan formation in South of Nalingelehe river, East Kunlun. *Contrib. Geol. Miner. Resour. Res.* **2017**, *32*, 245–253. (In Chinese with English Abstract)
48. Zhang, J.; Tang, H.W.; Hou, M.C.; Shi, J.B.; Yang, W.; Zhang, H.S.; Chen, L.; Ren, Q.J. Geochemistry and zircon U-Pb ages of the volcanic rocks in southern Galinge, Qinghai Province. *Geol. Bull. China* **2018**, *37*, 819–829. (In Chinese with English Abstract)
49. Zhao, M.F.; Shi, L.C.; Li, C.F.; Wei, Y.N.; Li, Y.L. Geochemistry and tectonic environment of the volcanic rocks from Elashan Formation in Zhong Juh area, Qinghai Province. *Geol. Resour.* **2018**, *27*, 117–123. (In Chinese with English Abstract)
50. Dou, G.Y.; Zhao, W.; Wang, Z.D.; Li, H.; Mao, J.Y. Geochemical Characteristics, Petrogenesis and Structural Setting of Late Triassic Epoch Rhyolite in Nageng Area, East Kunlun. *China's Mangan. Indust.* **2019**, *37*, 19–24. (In Chinese with English Abstract)
51. Yang, T.J.; Xi, D.H.; Zhang, K.Y. Petrogeochemistry and Tectonic Setting of Volcanic Rock of the Upper Triassic Elashan Formation in Xiangjiawugang, Elashan, Qinghai. *Acta Geol. Sichuan* **2019**, *39*, 187–194. (In Chinese with English Abstract)
52. Shao, F.L.; Niu, Y.L.; Kong, J.J.; Liu, Y.; Wang, G.D.; Zhang, Y. Petrogenesis and tectonic implications of the Triassic rhyolites in the East Kunlun Orogenic Belt, northern Tibetan Plateau. *Geosci. Front.* **2021**, *12*, 101243.
53. Zhu, Y.X.; Wang, L.X.; Ma, C.Q.; He, Z.X.; Deng, X.; Tian, Y. Petrogenesis and tectonic implication of the Late Triassic A1-type alkaline volcanics from the Xiangride area, eastern segment of the East Kunlun Orogen (China). *Lithos* **2022**, *412–413*, 106595.
54. McCulloch, M.T.; Kyser, T.K.; Woodhead, J.D.; Kinsley, L. Pb-Sr-Nd-O isotopic constraints on the origin of rhyolites from the Taupo Volcanic Zone of New Zealand: Evidence for assimilation followed by fractionation from basalt. *Contrib. Mineral. Petrol.* **1994**, *115*, 303–312.
55. Feeley, T.C.; Dungan, M.A. Compositional and dynamic controls on mafic-silicic magma interactions at continental arc volcanoes: Evidence from Cordón El Guadal, TatarA-San Pedro Complex, Chile. *J. Petrol.* **1996**, *37*, 1547–1577.
56. Pankhurst, R.J.; Riley, T.R.; Fanning, C.M.; Kelley, S.P. Episodic silicic volcanism in Patagonia and the Antarctic Peninsula: Chronology of magmatism associated with the break-up of Gondwana. *J. Petrol.* **2000**, *41*, 605–625.

57. Riley, T.R.; Leat, P.T.; Pankhurst, R.J.; Harris, C. Origins of large volume rhyolitic volcanism in the Antarctic Peninsula and Patagonia by crustal melting. *J. Petrol.* **2001**, *42*, 1043–1065.
58. Miller, J.A.; Harris, C. Petrogenesis of the Swaziland and northern natal rhyolites of the Lebombo Rifted volcanic margin, south east Africa. *J. Petrol.* **2007**, *48*, 185–218.
59. Annen, C.; Blundy, J.D.; Sparks, R.S.J. The genesis of intermediate and silicic magmas in deep crustal hot zones. *J. Petrol.* **2006**, *47*, 505–539.
60. Yin, H.F.; Zhang, K.X.; Chen, N.S.; Wang, G.C. *Regional Geological Report of the Peoples Republic of China: Donggi Conag Hu Map (147 C 001002), Scale 1:250,000*; China University of Geosciences Press: Wuhan, China, 2003; pp. 1–457. (In Chinese)
61. Liu, Y.S.; Hu, Z.C.; Zong, K.Q.; Gao, C.G.; Gao, S.; Xu, J.; Chen, H.H. Reappraisal and refinement of zircon U-Pb isotope and trace element analyses by LA-ICP-MS. *Chin. Sci. Bull.* **2010**, *55*, 1535–1546.
62. Andersen, T. Correlation of common lead in U-Pb analyses that do not report ^{204}Pb . *Chem. Geol.* **2002**, *192*, 59–79.
63. Ludwig, K.R. User's Manual for Isoplot/Ex Version 3.00. A Geochronological Toolkit for Microsoft Excel. *Berkeley Geochronol. Cent. Spec. Publ.* **2003**, *4*, 1–70.
64. Li, H.K.; Geng, J.Z.; Hao, S.; Zhang, Y.Q.; Li, H.M. Determination of U-Pb isotopic ages of zircons by LA-MC-ICPMS. *Acta Mineral. Sin.* **2009**, *29* (Suppl. S1), 600–601. (In Chinese with English Abstract)
65. Belousova, E.A.; Griffin, W.L.; Suzanne, G.W.; O'Reilly, S.Y.; Fisher, N.I. Igneous zircon: Trace element composition as an indicator of source rock type. *Contrib. Mineral. Petr.* **2002**, *143*, 602–622.
66. Wu, Y.B.; Zheng, Y.F. Genesis of zircon and its constraints on interpretation of U-Pb age. *Chin. Sci. Bull.* **2004**, *49*, 1554–1569.
67. Siebel, W.; Blaha, U.; Chen, F.K.; Johann, R. Geochronology and geochemistry of a dyke-host rock association and implications for the formation of the Bavarian Pfahl shear zone, Bohemian Massif. *Int. J. Earth Sci.* **2005**, *94*, 8–23.
68. Hoskin, P.W.O.; Black, L.P. Metamorphic zircon formation by solid-state recrystallization of protolith igneous zircon. *J. Metamorph. Geol.* **2000**, *18*, 423–439.
69. Middlemost, E.A.K. Naming materials in the magma/igneous rock system. *Earth-Sci. Rev.* **1994**, *37*, 215–224.
70. Rickwood, P.C. Boundary lines within petrologic diagrams which use oxides of major and minor elements. *Lithos* **1989**, *22*, 247–263.
71. Frost, C.D.; Frost, B.R. On ferroan (A-type) granitoids: Their compositional variability and modes of origin. *J. Petrol.* **2010**, *52*, 39–53.
72. Maniar, P.D.; Piccoli, P.M. Tectonic Discrimination of Granitoids. *Geol. Soc. Am. Bull.* **1989**, *101*, 635–643.
73. Sun, S.S.; McDonough, W.F. Chemical and isotopic systematics of oceanic basalt: Implications for mantle composition and processes. *Geol. Soc. Lond. Spec. Publ.* **1989**, *42*, 313–345.
74. Ding, S.; Huang, H.; Niu, Y.L.; Zhao, Z.D.; Yu, X.H.; Mo, X.X. Geochemistry, geochronology and petrogenesis of East Kunlun high Nb-Ta rhyolites. *Acta Petrol. Sin.* **2011**, *27*, 3603–3614. (In Chinese with English Abstract)
75. Loiselle, M.C.; Wones, D.R. Characteristics and origin of an orogenic granites. *Geol. Soc. Am. Abstr. Prog.* **1979**, *11*, 468.
76. Sun, Y.; Ma, C.Q.; Liu, Y.Y.; She, Z.B. Geochronological and geochemical constraints on the petrogenesis of Late Triassic aluminous A-type granites in Southeast China. *J. Asian Earth Sci.* **2011**, *42*, 1117–1131.
77. Wang, K.X.; Sun, T.; Chen, P.R.; Ling, H.F.; Xiang, T.F. The geochronological and geochemical constraints on the petrogenesis of the Early Mesozoic A-type granite and diabase in northwestern Fujian Province. *Lithos* **2013**, *179*, 364–381.
78. Zhao, K.D.; Jiang, S.Y.; Chen, W.F.; Chen, P.R.; Ling, H.F. Zircon U-Pb chronology and elemental and Sr-Nd-Hf isotope geochemistry of two Triassic A-type granites in South China: Implication for petrogenesis and Indosinian transtensional tectonism. *Lithos* **2013**, *160–161*, 292–306.
79. Eby, G.N. The A-type granitoids: A review of their occurrence and chemical characteristics and speculations on their petrogenesis. *Lithos* **1990**, *26*, 115–134.
80. Eby, G.N. Chemical subdivision of the A-type granitoids: Petrogenetic and tectonic implications. *Geology* **1992**, *20*, 641–644.
81. Bonin, B. A-type granites and related rocks: Evolution of a concept, problems and prospects. *Lithos* **2007**, *97*, 1–29.
82. King, P.L.; White, A.J.R.; Chappell, B.W.; Allen, C.M. Characterization and origin of aluminous A-type granites from the Lachlan Fold Belt, southeastern Australia. *J. Petrol.* **1997**, *38*, 371–391.
83. Jia, X.H.; Wang, Q.; Tang, G.J. A-type granites: Research progress and implications. *Geotect. Metallog.* **2009**, *33*, 465–480. (In Chinese with English Abstract)
84. Whalen, J.B.; Curie, K.L.; Chappell, B.W. A-type granites: Geochemical characteristics, discrimination and petrogenesis. *Contrib. Mineral. Petrol.* **1987**, *95*, 407–419.
85. Watson, E.B.; Harrison, T.M. Zircon saturation revisited: Temperature and composition effects in a variety of crustal magma types. *Earth Planet. Sci. Lett.* **1983**, *64*, 295–304.
86. Pearce, J.A.; Harris, N.B.W.; Tindle, A.G. Trace element discrimination diagrams for the tectonic interpretation of granitic rocks. *J. Petrol.* **1984**, *25*, 956–983.
87. Wu, F.Y.; Li, X.H.; Yang, J.H.; Zheng, Y.F. Discussions on the petrogenesis of granites. *Acta Petrol. Sin.* **2007**, *23*, 1217–1238. (In Chinese with English Abstract)
88. Collins, W.J.; Beams, S.D.; White, A.J.R.; Chappell, B.W. Nature and origin of A-type granites with particular reference to south-eastern Australia. *Contrib. Mineral. Petrol.* **1982**, *80*, 189–200.
89. DePaolo, D.J. A neodymium and strontium isotopic study of the Mesozoic calc-alkaline granitic batholiths of the Sierra Nevada and Peninsular Ranges, California. *J. Geophys. Res.* **1981**, *86*, 10470–10488.

90. Be'eri-Shlevin, Y.; Katzir, Y.; Blichert-Toft, J.; Kleinhanns, I.C.; Whitehouse, M.J. Nd-Sr-Hf-O isotope provinciality in the northernmost Arabian-Nubian Shield: Implications for crustal evolution. *Contrib. Mineral. Petrol.* **2010**, *160*, 181–201.
91. Weissman, A.; Kessel, R.; Navon, O.; Stein, M. The petrogenesis of calc-alkaline granites from the Elat massif, Northern Arabian-Nubian shield. *Precambrian Res.* **2013**, *236*, 252–264.
92. Yang, J.H.; Wu, F.Y.; Chung, S.L.; Wilde, S.A.; Chu, M.F. A hybrid origin for the Qianshan A-type granite, northeast China: Geochemical and Sr-Nd-Hf isotopic evidence. *Lithos* **2006**, *89*, 89–106.
93. Beard, J.S.; Lofgren, G.E. Effect of water on the composition of partial melts of greenstone and amphibolites. *Sci. Mag.* **1989**, *244*, 195–197.
94. Patiño Douce, A.E. Generation of metaluminous A-type granites by low-pressure melting of calc-alkaline granitoids. *Geology* **1997**, *25*, 743–746.
95. Bergantz, G.W. Underplating and partial melting: Implications for melt generation and extraction. *Science* **1989**, *245*, 1093–1095.
96. Roberts, M.P.; Clemens, J.D. Origin of high-potassium, calcalkaline, I-type granitoids. *Geology* **1993**, *21*, 825–828.
97. Droop, G.T.R.; Clemens, J.D.; Dalrymple, D.J. Processes and conditions during contact anatexis, melt escape and restite formation: The Hunly Gabbro complex, NE Scotland. *J. Petrol.* **2003**, *44*, 995–1029.
98. Lara, P.; Oyhantçabal, P.; Dadd, K. Post-collisional, Late Neoproterozoic, high-Ba-Sr granitic magmatism from the Dom Feliciano Belt and its cratonic foreland, Uruguay: Petrography, geochemistry, geochronology, and tectonic implications. *Lithos* **2017**, *277*, 178–198.
99. Gao, S.; Rudnick, R.L.; Yuan, H.L.; Liu, X.M.; Liu, Y.S.; Xu, W.L.; Ling, W.L.; John, A.; Wang, X.C.; Wang, Q.H. Recycling lower continental crust in the North China craton. *Nature* **2004**, *432*, 892–897.
100. Castro, A.; Moreno-Ventas, I.; De La Rosa, J.D. H-type (hybrid) granitoids: A proposed revision of the granite-type classification and nomenclature. *Earth-Sci. Rev.* **1991**, *31*, 237–253.
101. Qu, X.M.; Wang, H.N. Dynamic Study on the Crustalmantle Magma Mixing and Emplacement Mechanism of Guojialing Granite. *Chinese J. Geol.* **1997**, *32*, 445–454. (In Chinese with English Abstract)
102. Jiang, W.; Mo, X.X.; Zhao, C.H.; Guo, T.Y.; Zhang, S.Q. Geochemistry of granitoid and its mafic microgranular enclave in Gangdise belt, Qinghai-Xizang Plateau. *Acta Petrol. Sin.* **1999**, *15*, 89–97. (In Chinese with English Abstract)
103. Patiño Douce, A.E. What do experiments tell us about the relative contributions of crust and mantle to the origin of granitic magmas? *Geol. Soc. Lond. Spec. Publ.* **1999**, *168*, 55.
104. Xin, W.; Sun, F.Y.; Li, L.; Yan, J.M.; Zhang, Y.T.; Wang, Y.C.; Shen, T.S.; Yang, Y.J. The Wulonggou metaluminous A₂-type granites in the Eastern Kunlun Orogenic Belt, NW China: Rejuvenation of subduction-related felsic crust and implications for post-collision extension. *Lithos* **2018**, *312–313*, 108–127.
105. Chen, J.J.; Fu, L.B.; Wei, J.H.; Selby, D.; Zhang, D.H.; Zhou, H.Z.; Zhao, X.; Liu, Y. Proto-Tethys magmatic evolution along northern Gondwana: Insights from Late Silurian-Middle Devonian A-type magmatism, East Kunlun Orogen, Northern Tibetan Plateau, China. *Lithos* **2020**, *356–357*, 105304.
106. Dall'Agnol, R.; Scaillet, B.; Pichavant, M. An experimental study of a Lower Proterozoic A-type granite from the eastern Amazonian Craton, Brazil. *J. Petrol.* **1999**, *40*, 1673–1698.
107. McDonough, W.F.; Sun, S.S.; Ringwood, A.E.; Jagoutz, E.; Hofmann, A.W. Potassium, rubidium, and cesium in the earth and moon and the evolution of the mantle of the earth. *Geochim. Cosmochim. Acta* **1992**, *56*, 1001–1012.
108. Tischendorf, G.; Paelchen, W. Zur Klassifikation von Granitoiden. *Z. Geol. Wiss.* **1985**, *13*, 615–627.
109. Pearce, J.A. Role of sub-continental Lithosphere in magma genesis at active continental margins. In *Continental Basalts and Mantle Xenoliths*; Hawkesworth, C.J.; Norry, M.J., Eds.; Shiva Publications: Nantwich, UK, 1983; pp. 230–249.
110. Wilson, M. Review of igneous petrogenesis: A global tectonic approach. *Terra Nova* **1989**, *1*, 218–222.
111. Zorpi, M.J.; Coulon, C.; Orsini, J.B. Hybridization between felsic and mafic magmas in calc-alkaline granitoids: A case study in northern Sardinia, Italy. *Chem. Geol.* **1991**, *92*, 45–86.
112. Jahn, B.M.; Wu, F.; Lo, C.H. Crust-mantle Interaction Induced by Deep Subduction of the Continental Crust: Geochemical and Sr-Nd Isotopic Evidence from Post-collisional Mafic-ultramafic Intrusions of the Northern Dabie Complex, Central China. *Chem. Geol.* **1999**, *157*, 119–146.
113. Taylor, S.R.; McLennan, S.M. *The Continental Crust: Its Composition and Evolution*; Blackwell Scientific: Oxford, UK, 1985; p. 312.
114. Pearce, J.A.; Bender, J.F.; DeLong, S.E. Genesis of Collision Volcanism in Eastern Anatolia, Turkey. *J. Volcanol. Geoth. Res.* **1990**, *44*, 189–229.
115. Harris, N.B.W.; Pearce, J.A.; Tindle, A.G. Geochemical characteristics of collision-zone magmatism. In *Collision Tectonics Geological Society*; Coward, M.P., Reis, A.C., Eds.; Special Publications: London, UK, 1986; Volume 19, pp. 67–81.
116. Thiéblemont, D.; Tegye, M. Geochemical discrimination of differentiated magmatic rocks attesting for the variable origin and tectonic setting of calc-alkaline magmas. *Comptes Rendus L'académie Des Sci. Ser. II* **1994**, *319*, 87–94.
117. Clemens, J.D.; Holloway, J.R.; White, A.J.R. Origin of an A-type granite: Experimental constraints. *Am. Mineral.* **1986**, *71*, 317–324.
118. Hong, D.W.; Wang, S.G.; Han, B.F. *Two Types of Alkaline Granite and Their Discrimination: Volume 28 Collected Works of Institute of Geology*; Chinese Academy of Geological Sciences: Beijing, China, 1995; pp. 123–124. (In Chinese with English Abstract)
119. Zhang, Q.; Ran, H.; Li, C.D. A-type granite: What is the essence? *Acta Petrol. Miner.* **2012**, *31*, 621–626. (In Chinese with English Abstract)

120. Jiang, C.F.; Yang, J.S.; Feng, B.G.; Zhu, Z.Z.; Zhao, M.; Chai, Y.C. *Opening Closing Tectonics of Kunlun Mountains*; Geological Publishing House: Beijing, China, 1992; pp. 217, (In Chinese).
121. Yang, J.S.; Xu, Z.Q.; Li, H.B.; Shi, R.D. The Paleo-Tethys volcanism and plate tectonic regime in the A'nyemaqen region of East Kunlun, northern Tibet Plateau. *Acta Petrol. Miner.* **2005**, *24*, 369–380. (In Chinese with English Abstract)
122. Guo, Z.F.; Deng, J.F.; Xu, Z.Q.; Mo, X.X.; Luo, Z.H. Late Palaeozoic-Mesozoic intracontinental orogenic process and intermediate-acidic igneous rocks from the Eastern Kunlun Mountains of northwestern China. *Geosciences* **1998**, *12*, 344–352. (In Chinese with English Abstract)
123. Yuan, W.M.; Mo, X.X.; Yu, X.H.; Luo, Z.H. The Record of Indosinian Tectonic Setting from the Granotoid of Eastern Kunlun Mountains. *Geol. Rev.* **2000**, *46*, 203–211. (In Chinese with English Abstract)
124. Sun, Y.; Pei, X.Z.; Ding, S.P.; Li, R.B.; Feng, J.Y.; Zhang, Y.F.; Li, Z.C.; Chen, Y.X.; Zhang, X.F.; Chen, G.C. Halagatu magma mixing granite in the East Kunlun Mountains: Evidence from Zircon U-Pb dating. *Acta Geol. Sin.* **2009**, *83*, 1000–1010. (In Chinese with English Abstract)
125. Huang, H.; Niu, Y.L.; Nowell, G.; Zhao, Z.D.; Yu, X.H.; Zhu, D.C.; Mo, X.X.; Ding, S. Geochemical constraints on the petrogenesis of granitoids in the East Kunlun Orogenic belt, northern Tibetan Plateau: Implications for continental crust growth through syn-collisional felsic magmatism. *Chem. Geol.* **2014**, *370*, 1–18.
126. Kong, J.J.; Niu, Y.L.; Hu, Y.; Zhang, Y.; Shao, F.L. Petrogenesis of the Triassic granitoids from the East Kunlun Orogenic Belt, NW China: Implications for continental crust growth from syn-collisional to post-collisional setting. *Lithos* **2020**, *364–365*, 105513.
127. Li, Z.C.; Pei, X.Z.; Li, R.B.; Pei, L.; Chen, Y.X.; Liu, C.J.; Liu, Z.Q.; Chen, G.C.; Wang, M.; Zhao, S.W. The latest tectonic magmatism in the Buqingshan-A'nyemaqen tectonic mélange belt: Evidence from zircon U-Pb geochronology of intermediate-basic dikes, northern Tibetan Plateau, China. *Arab. J. Geosci.* **2019**, *12*, 374.
128. Yu, S.Y.; Peng, Y.B.; Zhang, J.X.; Li, S.Z.; Santosh, M.; Li, Y.S.; Liu, Y.J.; Gao, X.Y.; Ji, W.T.; Lv, P.; et al. Tectono-thermal evolution of the Qilian orogenic system: Tracing the subduction, accretion and closure of the Proto-Tethys Ocean. *Earth-Sci. Rev.* **2021**, *215*, 103547.
129. Peng, Y.B.; Yu, S.Y.; Li, S.Z.; Zhang, J.X.; Liu, Y.J.; Li, Y.S.; Santosh, M. Early Neoproterozoic magmatic imprints in the Altun-Qilian-Kunlun region of the Qinghai-Tibet Plateau: Response to the assembly and breakup of Rodinia supercontinent. *Earth-Sci. Rev.* **2019**, *199*, 102954.
130. Condie, K.C. Trace-element geochemistry of Archean greenstone belts. *Earth-Sci. Rev.* **1976**, *12*, 393–417.
131. Liegeois, J.P.; Navez, J.; Hertogen, J.; Black, R. Contrasting origin of post-collisional high-K calc-alkaline and shoshonitic versus alkaline and peralkaline granitoids: The use of sliding normalization. *Lithos* **1998**, *45*, 1–28.
132. Li, Z.C.; Pei, X.Z.; Liu, Z.Q.; Li, R.B.; Pei, L.; Chen, G.C.; Liu, C.J.; Chen, Y.X.; Gao, J.M.; Wei, F.H.; et al. Geochronology and geochemistry of the Gerizhuotuo diorites from the Buqingshan tectonic mélange belt in the southern margin of East Kunlun and their geologic implications. *Acta Geol. Sin.* **2013**, *87*, 1090–1103. (In Chinese with English Abstract)
133. Huang, J. *Late Triassic Tectonic Extension in East Kunlun Mountains: Evidence from Binggou Basic Dyke Group*; China University of Geosciences: Wuhan, China, 2013.
134. Luo, M.F.; Mo, X.X.; Yu, X.H.; Li, X.W.; Huang, X.F.; Yu, J.C. Zircon LA-ICP-MS U-Pb age dating, petrogenesis and tectonic implications of the Late Triassic granites from the Xiangride area, East Kunlun. *Acta Petrol. Sin.* **2014**, *30*, 3229–3241. (In Chinese with English Abstract)
135. Ao, C.; Sun, F.Y.; Li, B.L.; Wang, G.; Li, L.; Li, S.J.; Zhao, J.W. U-Pb dating, geochemistry and tectonic implications of Xiaojianshan gabbro in Qimantage mountain, Eastern Kunlun orogenic belt. *Geotect. Metallog.* **2015**, *39*, 1176–1184. (In Chinese with English Abstract)
136. Li, X.W.; Huang, X.F.; Luo, M.F.; Dong, G.C.; Mo, X.X. Petrogenesis and geodynamic implications of the Mid-Triassic lavas from East Kunlun, northern Tibetan Plateau. *J. Asian Earth Sci.* **2015**, *105*, 32–47.
137. Deng, W.B.; Pei, X.Z.; Liu, C.J.; Li, Z.C.; Li, R.B.; Chen, Y.X.; Chen, G.C.; Yang, S.; Chen, G.; Sang, J.Z.; et al. LA-ICP MS zircon U-Pb dating of the Chahantaolegai syenogranites in Xiangride area of East Kunlun and its geological significance. *Geol. Bull. China* **2016**, *35*, 687–699. (In Chinese with English Abstract)

Disclaimer/Publisher's Note: The statements, opinions and data contained in all publications are solely those of the individual author(s) and contributor(s) and not of MDPI and/or the editor(s). MDPI and/or the editor(s) disclaim responsibility for any injury to people or property resulting from any ideas, methods, instructions or products referred to in the content.